

Elastic fractal higher-order topological states

Tingfeng Ma, Bowei Wu, Jiachao Xu, Hui Chen^{*}, Shuanghuizhi Li, Boyue Su,
Pengfei Kang

School of Mechanical Engineering and Mechanics, Ningbo University, Ningbo 315211,
China

ABSTRACT

In this work, elastic fractal higher-order topological states are investigated. Bott index is adopted to characterize the topological property of elastic fractal structures. The topological corner and edge states of elastic waves in fractal structures are realized theoretically and experimentally. Different from traditional two-dimension (2D) high-order topological insulators based on periodic structures, the high-order topological states based on elastic fractal structures in this work intuitively reflect the fractal dimension in physics, supporting not only abundant topological outer corner states, but also rich inner corner states. The richness of corner states is much higher than that of topological insulators based on periodic structures. The strong robustness of the topological corner states in the fractal structure are verified by introducing disorders and defects. The topological phenomenon of in elastic fractal structures revealed in this work enriches the topological physics of elastic systems and breaks the limitation of that relies on periodic elastic structures. The results have important application prospects in energy harvesting, information transmissions, elastic energy acquisitions and high-sensitivity detections.

Key words: Elastic fractal; Higher-order topological states; Bott index; Robustness

1.Introduction

In recent years, topological insulators[1–3] have shown great potentials in wave transmission controls, which can realize wave transmissions with extremely low loss and the transmission effect is not sensitive to structural defects. Topological insulators have been successfully applied in fields of electromagnetic[4–6], acoustic[7–11], elastic waves[12–15].

Topological transmission brings important opportunities for elastic wave communications and sensing by improving signal-to-noise ratios and resolutions[16,17]. Specially, the reconfigurable zero-dimensional (0D) localized resonances with high energy-aggregation can be realized by using the high-order topological states of elastic waves. Fan et al. [18] realized the higher-order topological states in a two-dimensional (2D) continuous elastic system, experimentally observed the gapped one-dimensional (1D) edge states, the trivially gapped 0D corner states, and the topologically protected 0D corner states. Hong et al. [19] explored the valley-selectivity of corner states at high frequencies by engineering positions of the valley polarization, which provides generality for realizing high-frequency edge states and corner states. Liu et al. [20] investigates the higher-order topological behavior of elastic wave metamaterials composed of L-shaped pillars attached to a plate, and realized physical transferring among the corner, edge, and bulk elastic

wave modes by tuning the rotation angle of the L-shaped pillars.

For higher-order topological states, previous studies mostly focused only on systems in an integer-dimension, namely periodic systems satisfying the Bloch's theorem. However, the number of higher-order topological states generated in periodic systems is very limited, which cannot provide rich topological states required in applications. In recent years, the higher order topological states generated in fractal systems in a non-integer dimension have received much attentions.

Fractal [21] is a geometric form with self-similarity, and its unique structure and properties provide a new idea of for metamaterial designs and acoustic wave controls. Based on fractal, many fascinating topological phenomena have been discovered[22–24]. Biesenthal et al. [25] study fractal photonic topological insulators based on exact fractals composed exclusively of edge sites. Yang et al.[26] proved that photonic fractal Floquet topological insulators can be realized in photonic lattice with Sierpinski carpet composed of spiral optical waveguides. Zheng et al.[27] et al. found that the number of edge and corner states of fractal structures is much larger than that of traditional 2D periodic systems, and rich wave patterns of the corner states are verified. Li et al. [28] observe the one-way edge states that are protected by a robust mobility gap and demonstrates the fundamental interplay between the fractality and topological Haldane insulator. They[29] also experimentally realized

HOTI in an acoustical lattice and found that there exists a plenty of corner states.

However, the studies of higher-order topological phenomena based on fractal structures are currently limited to the fields of photonic[30–32] and acoustic waves[27,29]. In elastic systems, rich high-order topological corner and edge states are very important for realizing elastic wave sensing and communications with high resolution and stability. The topological states in elastic fractal structures have not been realized.

In this work, the elastic fractal higher-order topological states are investigated. The square and rhomboid fractal lattices are constructed, and Bott index is adopted to characterize the topological property of elastic fractal structures. Then, the higher order topological states of the square and rhombic fractal lattices are investigated numerically and experimentally, the robustness of which are further verified.

The structure of this paper is as follows: Section 2 presents the calculation of the Bott index for elastic waves in the fractal structure and explains the topological properties of the elastic fractal model; In section 3, the topological edge states and corner states of two fractal structure models are obtained by numerical simulation, and further verified by experiments; Section 4 verifies the robustness of topological elastic waves in fractal structures by introducing defects and lattice disorders; The conclusion is given in section 5.

2. Model and theory

The propagations of elastic waves in the fractal structure based on the square fractal shown in Fig. 1 (a) are considered. Through the box-counting method[33], the dimension number of the fractal model can be calculated (see the **Appendix A**): $d_f = \ln 8 / \ln 3 \approx 1.893$. The unit cell is shown in Fig. 1(b) and (c). The unit constant $a = 25\text{mm}$, the plate thickness and column thickness are respectively $h_1 = 2\text{ mm}$ and $h_2 = 6\text{ mm}$. Here the higher-order couplings are ignored, such as the next adjacent coupling[34–36]. In this work, the coupling strength is varied by changing the distance between the lattice points. The intra(inter)-coupling of the unit is controlled by the size of parameter $\beta = (d_2 - d_1) / a$, where $d_1(d_2)$ represents half of the distance of the intracellular (intercellular) units, respectively. In Fig.1 (b), the red dashed lines represent the shrinking-state lattice ($\beta > 0$) and the blue dashed lines represent the expanding-state lattice ($\beta < 0$). In order to further explain physical phase transitions in elastic lattice systems, the perturbative method[37] is used to obtain Hamiltonian as

$$\Delta \mathcal{H} \psi = \Delta \omega \psi \quad (1)$$

The Hamiltonian of the elastic system can be expressed as:

$$\mathcal{H} = \mathcal{H}_1 + \mathcal{H}_2. \quad (2)$$

Here

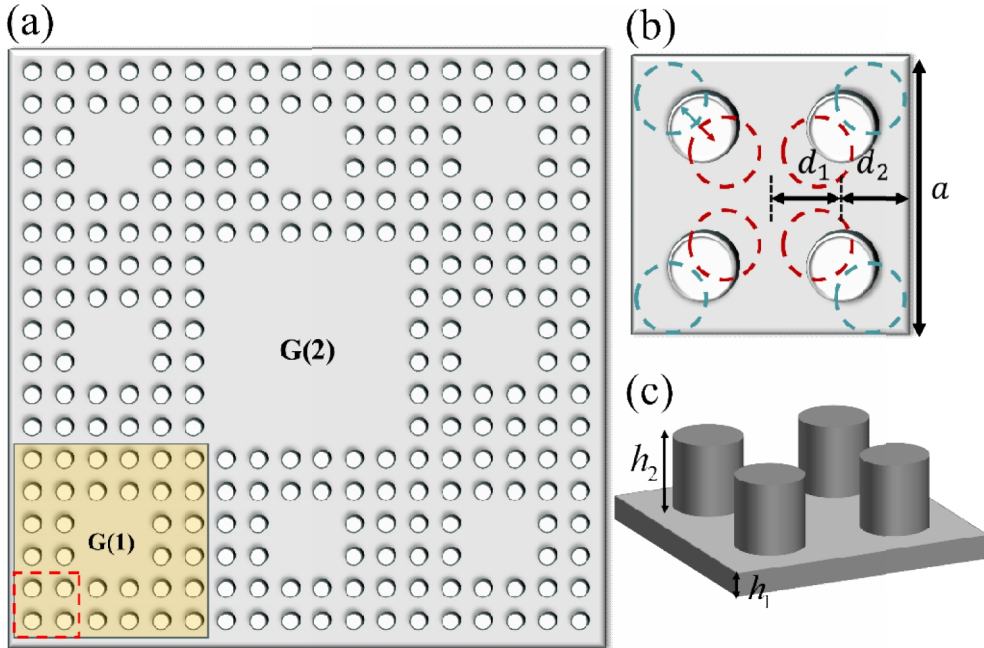
$$\mathcal{H}_1 = \begin{pmatrix} 0 & h_{12} & h_{13} & 0 \\ h_{12}^* & 0 & 0 & h_{24} \\ h_{13}^* & 0 & 0 & h_{34} \\ 0 & h_{24}^* & h_{34}^* & 0 \end{pmatrix} \quad (3)$$

where $h_{12} = t_a + t_b \exp(ik_x)$, $h_{13} = t_a + t_b \exp(-ik_y)$, $h_{24} = t_a + t_b \exp(-ik_y)$, and $h_{34} = t_a + t_b \exp(ik_x)$. The tight binding parameters $t_a \propto 1/d_1$ and $t_b \propto 1/d_2$ represent the intra-unit and inter-unit couplings between adjacent columns, respectively.

In our elastic system, each column represents a resonator, the Hamiltonian of each resonator can be expressed as:

$$\mathcal{H}_2 = \begin{pmatrix} \varepsilon_r & 0 & 0 & 0 \\ 0 & \varepsilon_r & 0 & 0 \\ 0 & 0 & \varepsilon_r & 0 \\ 0 & 0 & 0 & \varepsilon_r \end{pmatrix} \quad (4)$$

where ε_r is the vibration energy of a resonator which is determined by the resonant frequency (the value assigned to ε_r is 1).



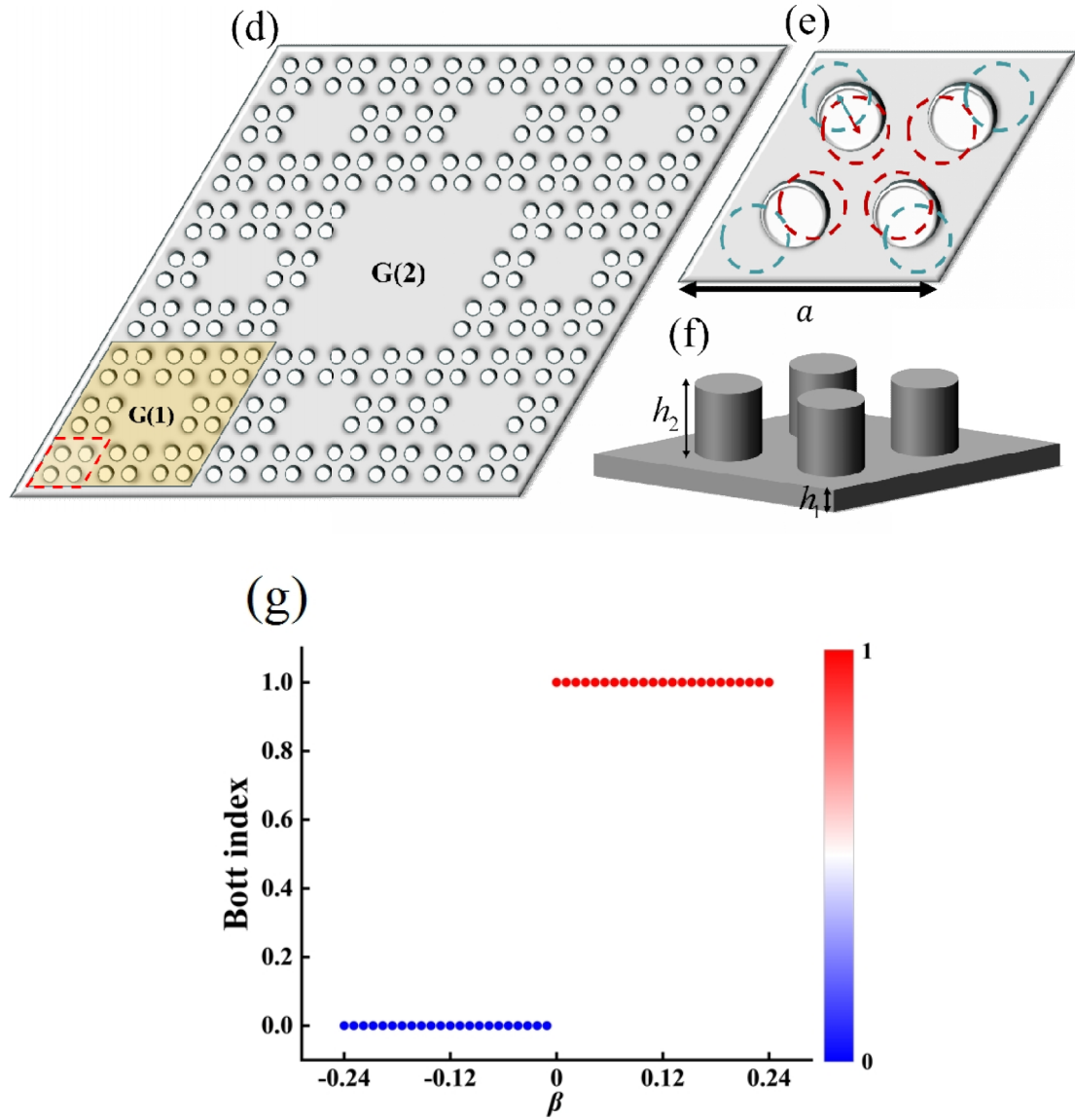


Fig. 1. Elastic fractal model. (a) Schematic of the square fractal structure. (b)-(c) Enlarged diagram of red frame of the square fractal structure. (d) Diagram of rhombus fractal model. (e)-(f) Enlarged diagram of red frame of rhombus fractal model. (g) The elastic Bott index of the square fractal structure vs. coupling strength. The topological phase transition is determined based on the Bott index, where the value of 1 indicates a topological nontrivial system, while the value of 0 represents a trivial system.

To further prove the existence of topological phase transitions in fractal models, it is necessary to characterize them by using topological invariants. However, the inheritance property of fractal structures makes it impossible to characterize that by using chern number[38–41] suitable

for periodic structures. Therefore, an invariant based on real space wavefunctions, the Bott index[42–45] is adopted to project the fractal lattice onto a two-dimensional space to characterize the fractal structure lacking a translation symmetry. The Bott index can be obtained from:

$$\nu_B = \frac{1}{2\pi} \text{Im} \left\{ \text{tr} [\log(UVU^\dagger V^\dagger)] \right\} \quad (4)$$

where U and V are given by

$$Pe^{i2\pi X}P = G \begin{pmatrix} 0 & 0 \\ 0 & U \end{pmatrix} G^\dagger \quad (5)$$

$$Pe^{i2\pi Y}P = G \begin{pmatrix} 0 & 0 \\ 0 & V \end{pmatrix} G^\dagger \quad (6)$$

where P is the projector on the occupied states, $e^{i2\pi X}$ and $e^{i2\pi Y}$ are diagonal unitary matrices. X and Y are the positional operators. G is a matrix whose columns are the eigenvectors of the Hamiltonian above.

The fractal structure shown in Fig. 1(a) is used as an example to calculate the Bott index, and the result (Bott index vs. β) is shown in Fig. 1(e). For the property of Bott index, the system is topologically protected when Bott index=1, while it is in a trivial state when Bott index=0. It can be seen from Fig. 1(e) that the system undergoes a topological phase transition when $\beta = 0$.

3. Elastic fractal higher-order topological states

In this section, the trivial and topological states of elastic waves in fractal structures are shown through a series of simulations and

experiments. In this work, only out-of-plane vibrations are considered, and free boundary conditions are imposed to the structure boundary.

3.1 Square fractal structures

3.1.1 Trivial states of square fractal structures

The simulation results of the eigenstates for $\beta = -0.08$ are shown in Fig. 2(a). For $\beta = -0.08$, the intracellular coupling is smaller than the intercellular coupling, thus the system is in a trivial state. Inner edge states, inner corner states and bulk states are represented by purple, green, and black dots, respectively. These inner edge and corner states are caused by the absence of lattice points in the structure, rather than a nontrivial state of the system. Analysis on periodic elastic structures in **Appendix D** verified this conclusion. Besides, in **Appendix D**, this is also verified by comparing the characteristics of fractal structures and non-fractal structure (some lattices are deleted randomly). Displacement distributions of bulk states (115.91kHz), inner edge states (95.059 kHz) and inner corner states (104.04 kHz) are respectively shown in Fig. 2(b), (c) and (d). For the bulk state, the energy is distributed throughout the structure and does not show an aggregation state; while for the inner corner state, the energy shows a certain aggregation state and gathers at the missing grid points of the fractal structure.

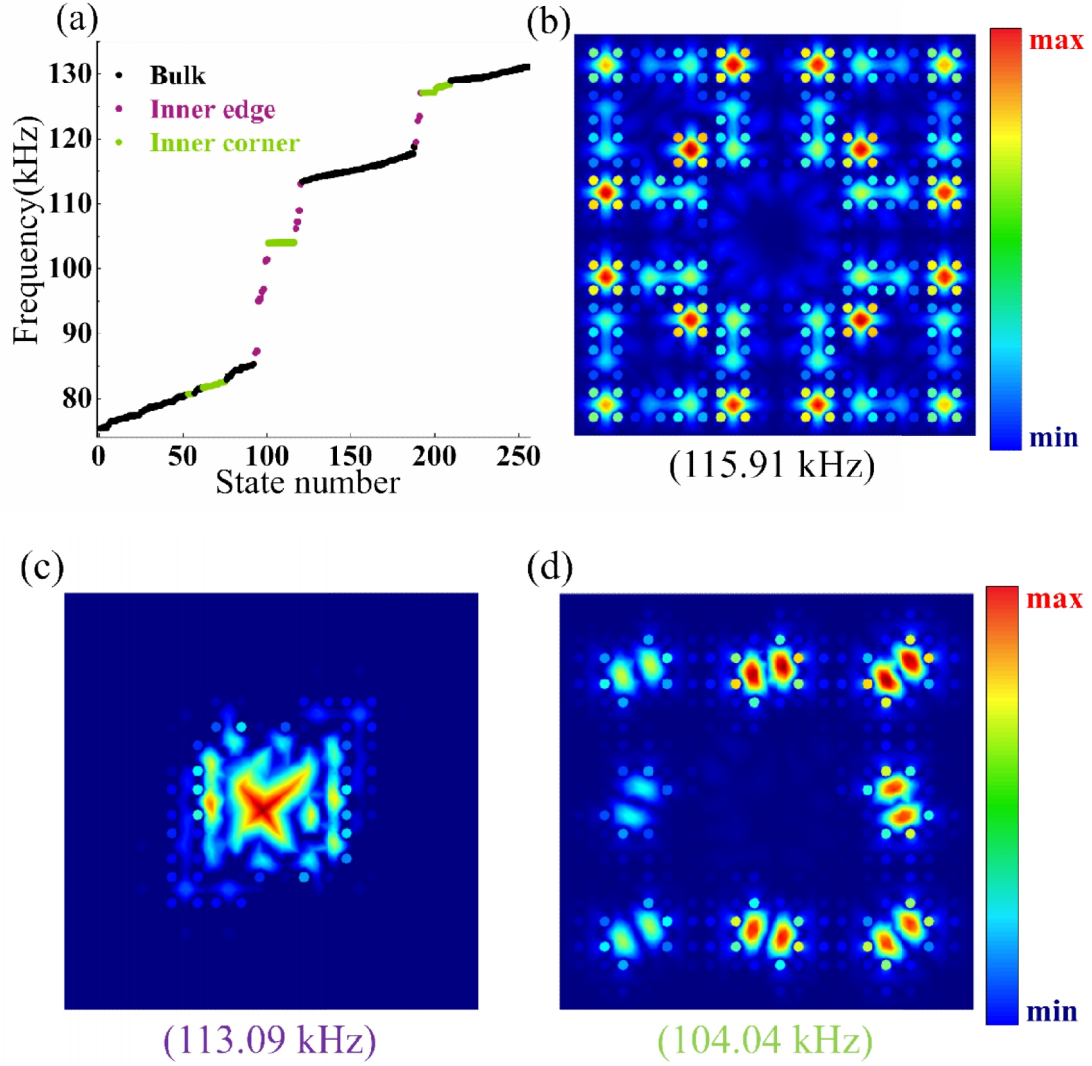
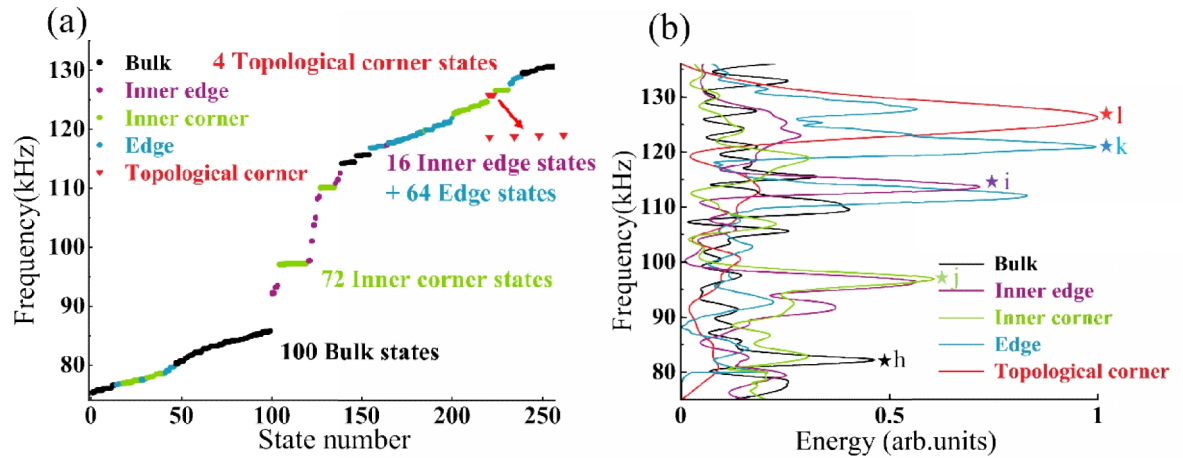


Fig. 2. Trivial system of square fractal model. (a) The eigenfrequency of the G (2) square fractal structure with a coupling parameter $\beta = -0.08$ obtained by simulations. Displacement distribution of eigenstates: (b) the bulk state at 115.91 kHz, (c) the inner edge states at 113.09 kHz, and (d) the inner corner states at 104.04 kHz.

3.1.2 Topological states of square fractal structures

For the coupling parameter $\beta = 0.08$, Bott index is 1. The simulation and experimental results of eigenstates of the system are shown in Fig. 3. In Fig. 3(a), there exists 100 bulk states (black), 72 inner corner states (green), 10 inner edge states (purple) and 70 outer edge states (blue). Besides, four topological corner states appear, represented

by the red inverted triangle. The positions of the inner corner states are roughly the same as those of the trivial states. Fig. 3(c)-(g) shows displacement distributions of the bulk states (82.217 kHz), inner edge states (112.63kHz), inner corner states (95.059kHz), and edge states (120.63kHz), topological corner states (126.00kHz) obtained by numerical simulations, respectively. It is shown that for topological edge and corner states, the energy is highly concentrated, and the four topological corner states have rotation symmetry, which proves the correctness of the calculation of the Bott index. The number of various states is consistent with the number calculated by the dimension. In addition, dimension numbers and eigenstates calculations are also carried out for the model of $G(3)$ states, and the results are shown in **Appendix A** and **Appendix B**.



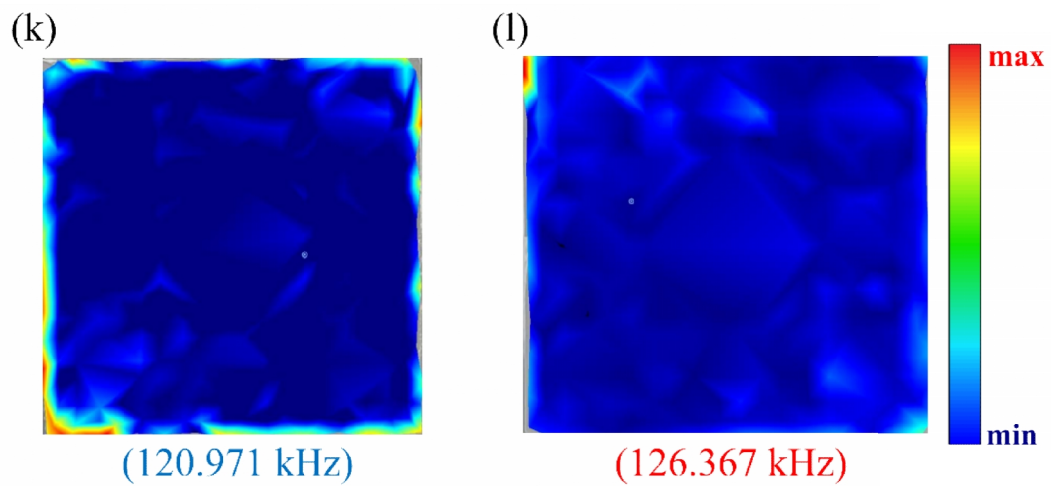
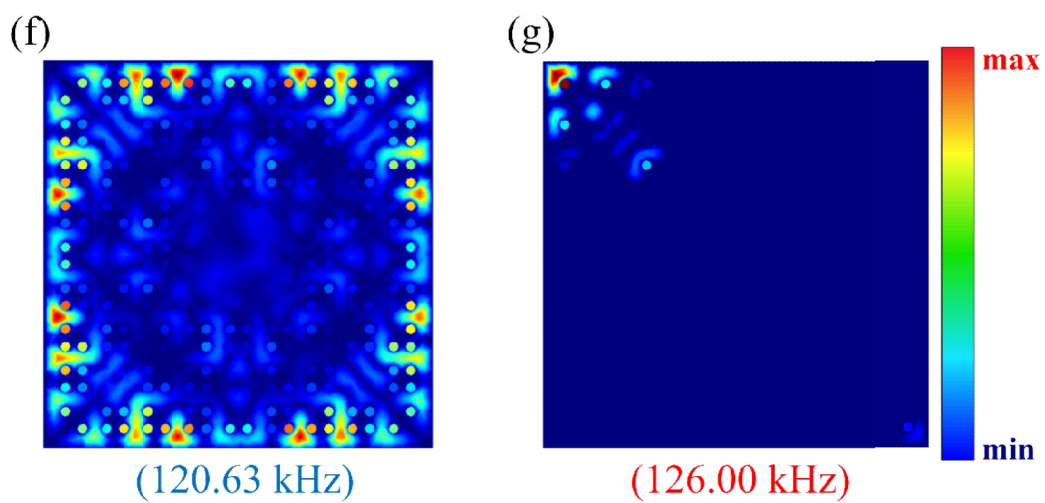
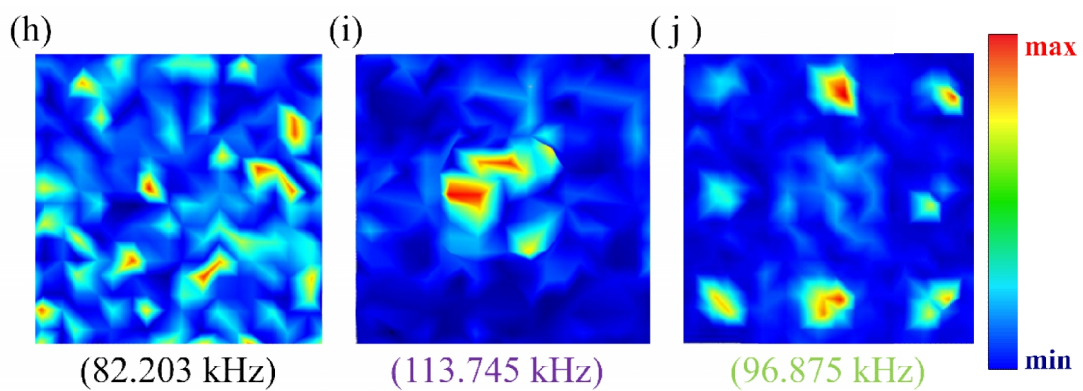
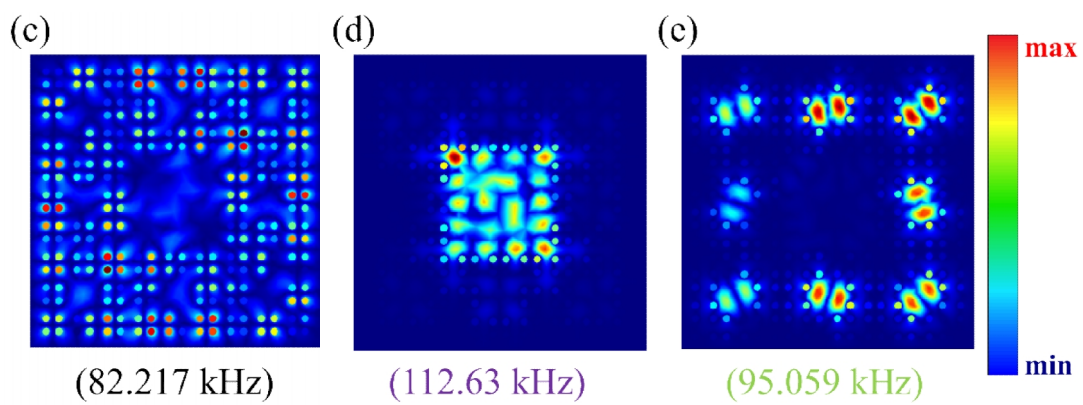


Fig. 3. Comparison between experimental and numerical simulations of topological non-trivial eigenstates of G (2) square fractal structures. (a) The eigenfrequency obtained for $\beta=0.08$ by simulation. (b) Normalized spectral diagram. (c)-(g) Simulation displacement distributions of the bulk state at 82.217kHz, the inner edge state at 112.63kHz, the inner corner state at 95.059kHz, the edge state at 120.63kHz and the topological corner state at 126.00kHz. (h)-(l) The experimental results of displacement distributions of the bulk state at 82.203kHz, the inner edge state at 113.745kHz, the inner corner state at 96.875kHz, the edge state at 120.971kHz and the topological corner state at 126.367kHz.

Elastic fractal plates are fabricated and the according tests are carried out to verify the simulation results. The material and structural parameters in experiments are the same as those in simulations (Section 2). The experimental test platform is shown in **Appendix C**.

The displacement response spectrums are normalized according to the maximum value, which are shown in Fig. 3(b). It can be seen that for the corner state and edge state, and the frequencies are close to the those obtained by numerical simulations in Fig. 3(a). Fig. 3(h)-(l) shows displacement distributions of bulk state (82.203kHz), inner edge state (113.745kHz), inner corner state (96.875kHz), and edge state (120.971kHz) and topological corner state (126.367kHz) obtained by experiments. It is shown that the experimental results are in good agreement with the simulation results.

3.2 Rhombus fractal structures

3.2.1 Trivial states of rhombus fractal structures

Eigenstates of the G(2) rhomboid fractal structure (Fig.1(b)) obtained by simulations are shown in Fig.4(a). When the intracellular

coupling is smaller than the intercellular coupling (expansion state), the system is in the trivial state. The purple, green and black dots represent the inner edge states, the inner corner states, and the bulk states, respectively. The appeared inner corner states are due to the characteristics of the structure itself, rather than a nontrivial state of the system. Displacement distributions of bulk states, inner states and corner states are shown in Figs. 4(b), (c) and (d), respectively. For bulk states, the energy is dispersed around and did not show an aggregation state, while for the inner edge and corner states, energy aggregation emerges in the positions where the lattice points of the fractal structure are missing.

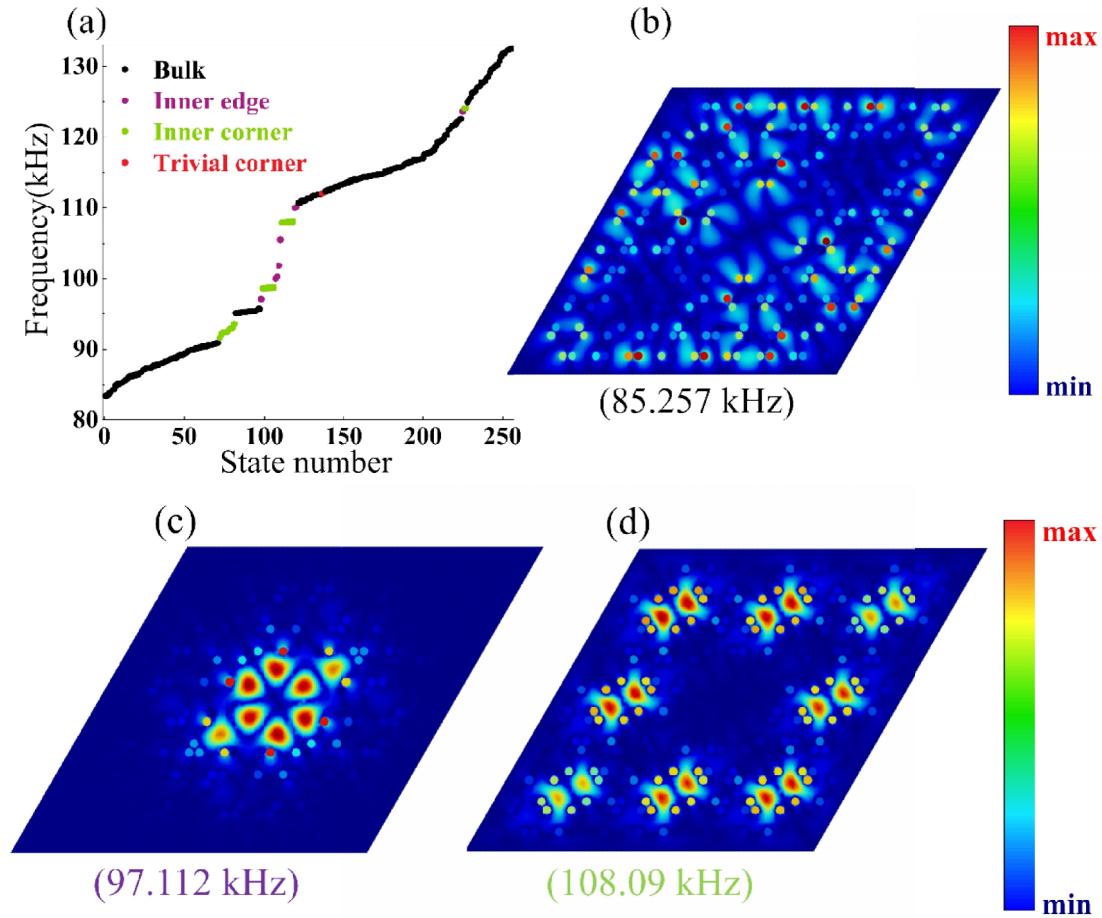


Fig. 4. Trivial system of square fractal model. (a) The eigenfrequency of the G (2)

rhombus fractal structure at the trivial state obtained by simulations. Displacement distribution of eigenstates: (b) The bulk state at 85.257 kHz, (c) The inner edge states at 97.112 kHz, (d) The inner corner states at 108.09 kHz.

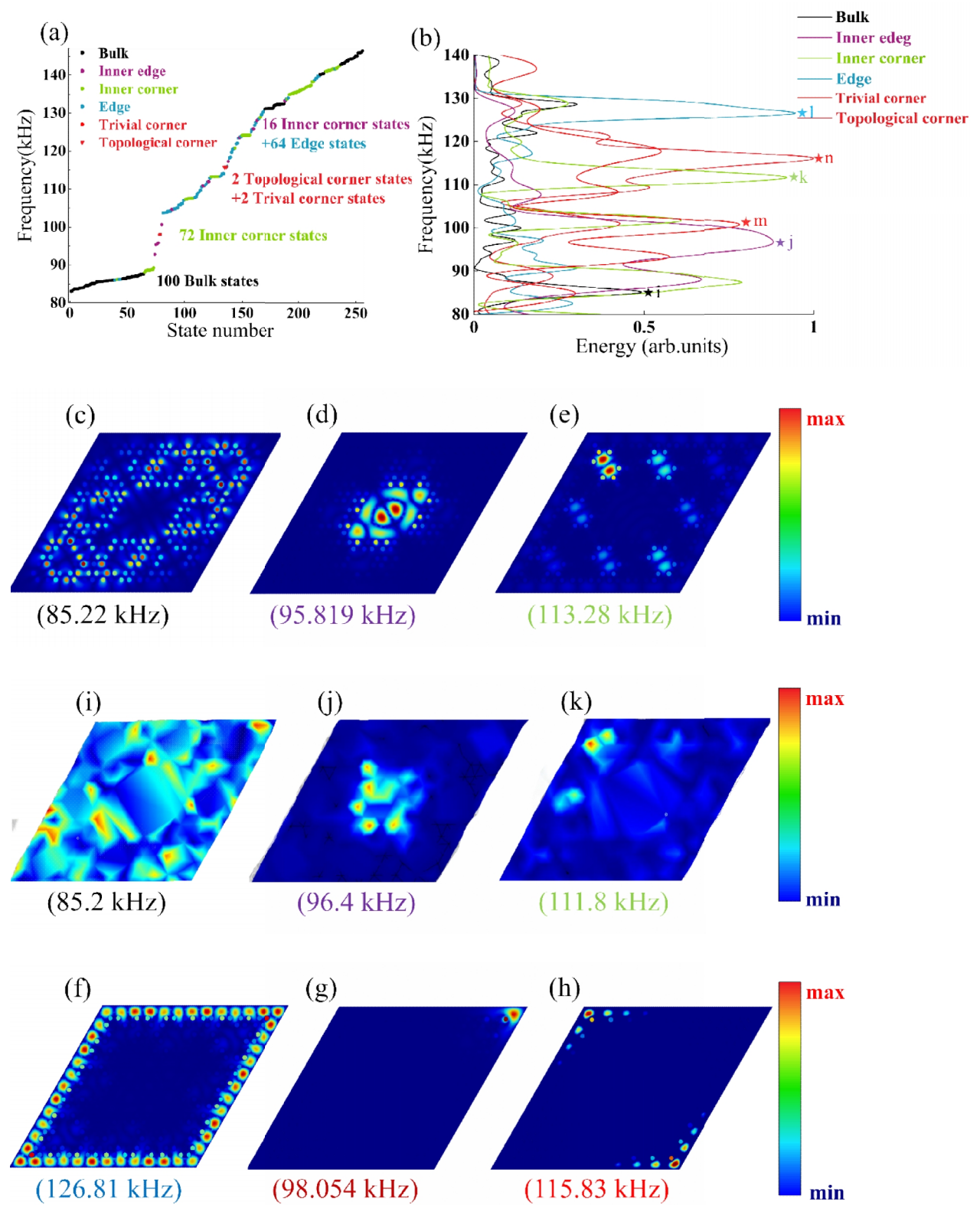
3.1.2 Topological states of rhombus fractal structures

Eigenstates of the G(2) rhomboid fractal structures (Fig. 1(b)) are numerically simulated, the results are shown in Fig.4(a). When the intracellular coupling is larger than the extracellular coupling, and the system enters the topological state. Fig.5(a) shows eigenstates obtained by simulations, bulk states, inner edge states, inner corner states, trivial corner states, topological corner states, and edge states are marked with black dots, purple dots, green dots, red dots, red inverted triangle and blue dots, respectively. Frequencies of the inner corner state in this case are roughly the same as those in the trivial system, and the band gap size increases significantly with the increase of intracellular coupling. Fig. 5(c)-(h) show displacement distributions of bulk state (85.22 kHz), inner edge state (95.819 kHz), inner corner state (113.28 kHz), edge state (126.81 kHz), trivial corner state (98.054 kHz) and topological corner state (115.83kHz) obtained by numerical simulations. It is shown that the energy of the edge state and corner state is highly concentrated, and the topological corner state appears at the $2\pi/3$ corner, and the trivial corner state appears at the $\pi/3$ corner (

Appendix

F explains the reason for the occurrence of the trivial corner states, and **Appendix G** experimentally proves that the trivial corner state does not

show topological robustness). In addition, the model of $G(3)$ are analyzed in Appendix B.



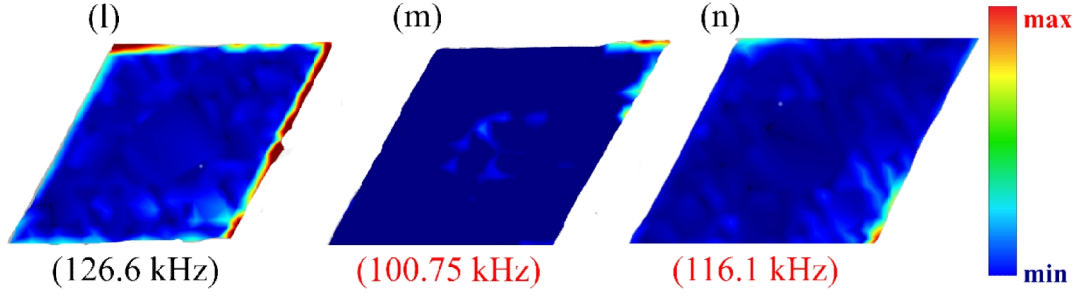


Fig. 5. Comparison between experimental and numerical simulations of topological non-trivial eigenstates of G (2) rhombus fractal structures. (a) The non-trivial eigenfrequency obtained by simulations. (b) Normalized spectral diagram. (c)-(g) Simulation displacement distributions of the bulk state at 85.22 kHz, the inner edge state at 95.819 kHz, the inner corner state at 113.28 kHz, the edge state at 126.81 kHz, the trivial corner state at 98.054 kHz and the topological corner state at 115.83 kHz. (h)-(l) The experimental results of displacement distributions of the bulk state at 85.2 kHz, the inner edge state at 96.4 kHz, the inner corner state at 111.8 kHz, the edge state at 126.6 kHz, trivial corner state at 100.75 kHz and the topological corner state at 116.1 kHz.

The fabricated rhombus fractal samples and the experimental platform are shown in Appendix C. The measured normalized response spectrum curve is shown in Fig. 5(b). It can be seen that the maximum energy appears at the topological corner state, while the energy value at the trivial corner state is small, and the corresponding frequencies are consistent with those obtained by numerical calculations.

Displacement distributions of bulk state (85.2 kHz), inner edge state (96.4 kHz), inner corner state (111.8 kHz), edge state (126.6 kHz), trivial corner state (100.75kHz) and topological corner state(116.1kHz) are shown in Fig.5 (i)-(n), respectively. For the bulk state, the displacement distribution is spread throughout the structure. For the inner corner state, the energy is still concentrated at the position where lattice points are missing. The energy of the edge state is concentrated around the edge.

The energy of trivial and topological corner states is less diffused, accumulating at the corner points. It is shown that the experimental results agree well with those obtained by simulations.

4. Analysis of the robustness

An important property of topological states is the robustness to defects. For $G(2)$ square and rhombic fractal structures, defects and disorders are set to verify the robustness of the topological edge and corner states. Disorders are also introduced by moving three columns to change the coupling strength, as shown in the inset of Fig. 7(a); Besides, the columns at the diagonal point are lengthened to introduce disorders, as shown in the inset in Fig. 7(b); For the defect setting, three columns near the corner points are deleted, as shown in the inset in Fig. 7(c). Fig. 7(d) shows the normalized energy spectrum curve of corner states obtained by experiments. The results show that after the introductions of defects and disorders in the $G(2)$ square fractal structure, although there is a small fluctuation for the frequency of corner states, and some energy spread to the edge, the energy is still concentrated near the corner point, and the peak frequency is almost unchanged, indicating that the introduction of defects and disorders have slight influence on the energy distributions of corner states.

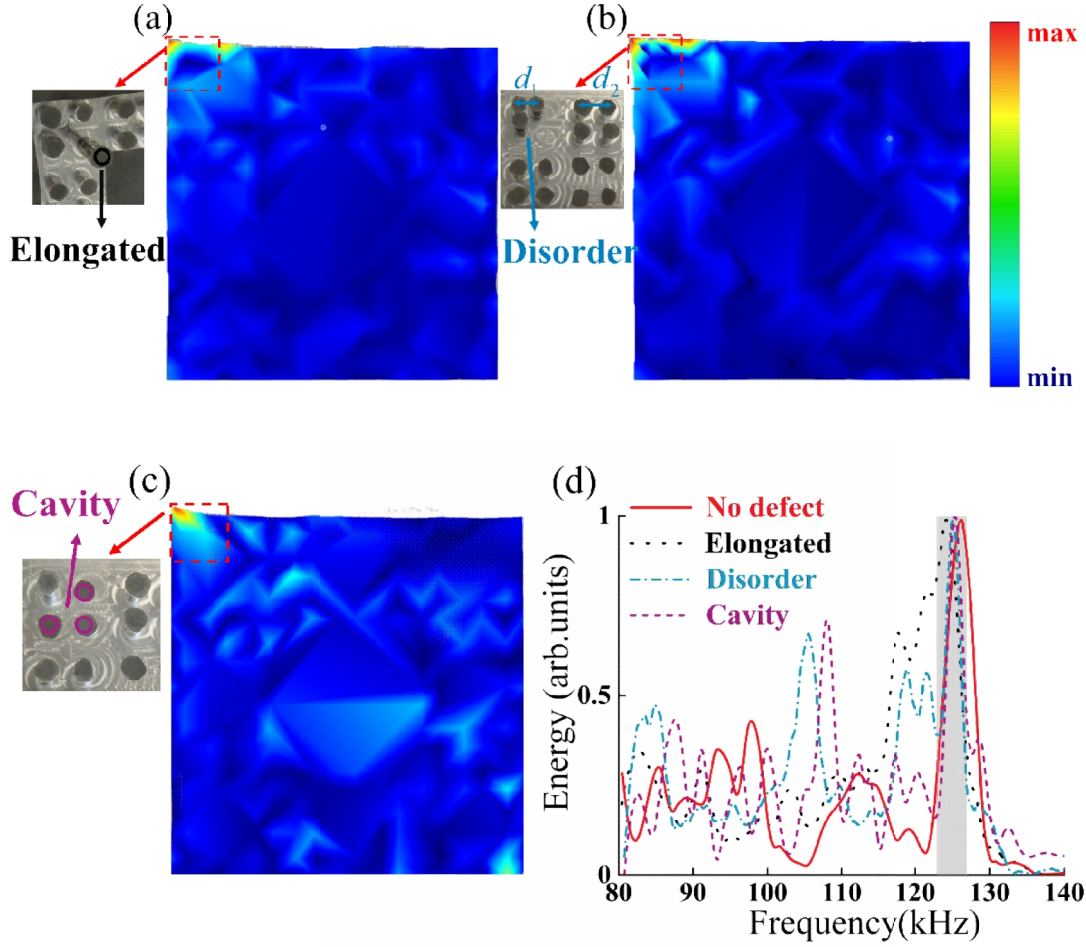


Fig. 4. Robustness verification of the G(2) square fractal structure. (a)-(c) perturbed model (**elongated**), perturbed model (disordered), model with cavity (three columns are deleted). (d) Normalized energy spectra.

For the rhomboid fractal structure of G(2), defects and disorders are introduced in the same way as that for the square fractal structure, the displacement distributions are shown in Fig. 8. It is shown that after the disorders are introduced, the energy accumulation effect at the corner state is basically unchanged. In addition, it can be seen from the normalized energy spectrum curve (Fig.8(d)) that the peak frequency of defects is slightly offset after the disorders are introduced. The

experimental results show that the topological corner states of the two fractal models in elastic systems are not sensitive to defects and disorders.

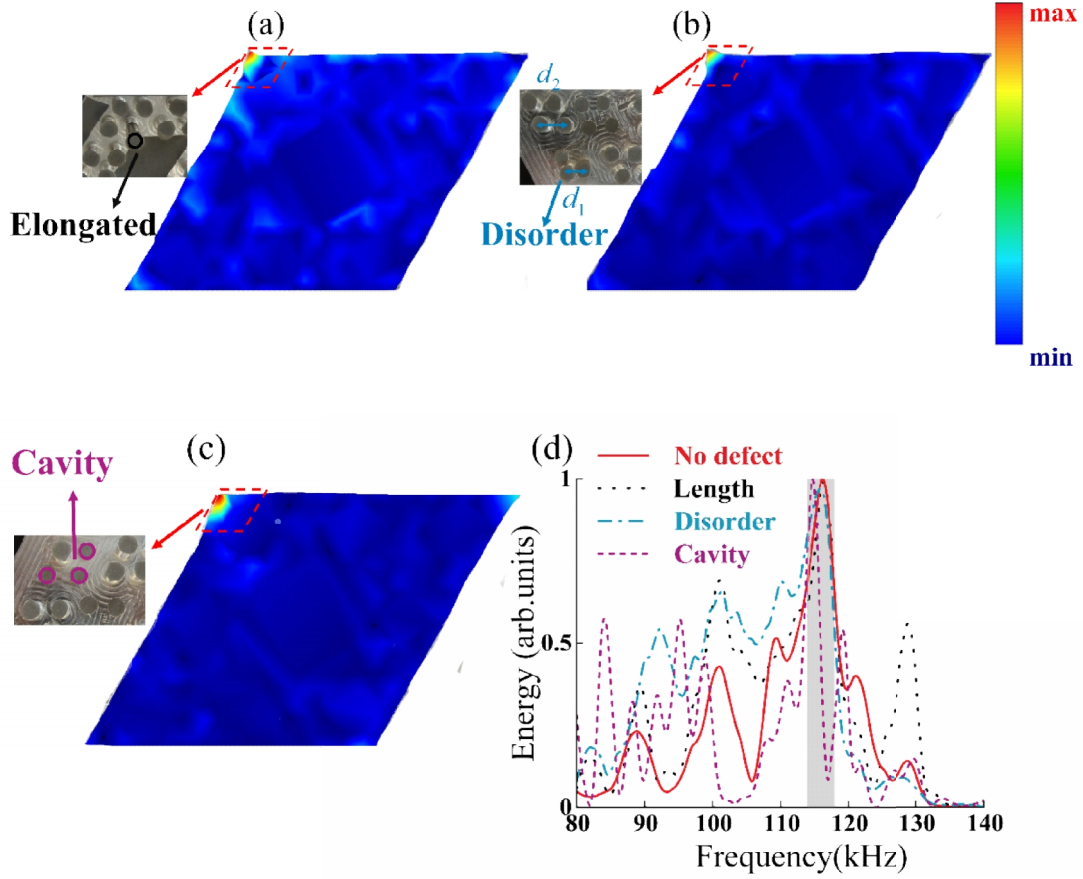


Fig. 8. Robustness verification of the G(2) rhombus fractal structure. (a)-(c) perturbed model (**elongated**), perturbed model (**disordered**), model with cavity (three columns are deleted). (d) Normalized energy spectra.

5. Conclusions

In this work, the topological phenomenon of elastic waves in the fractal structure are investigated through simulation and experimental methods. Elastic plates based on fractal structures are designed. By changing the distance between lattice points, the coupling strength are adjusted, the topological corner and boundary states of elastic waves based on fractal structures are realized. Different from traditional 2D

higher-order topological insulators based on periodic structures, the higher-order topological states based on elastic fractal structures in this work intuitively reflect the fractal dimension in physics, supporting not only the outer corner states with topological protections, but also rich inner corner states and boundary states, and the richness of corner states is much higher than that of topological insulators based on periodic structures. The strong robustness of the topological corner states in the fractal structures are verified by introducing disorders and defects.

The topological phenomenon of in elastic fractal structures revealed in this work enriches the topological physical properties of elastic systems and breaks the limitation of that relies on periodic elastic structures. Topological phenomena based on fractal structures can be applied in elastic wave energy locations, information transmissions, high-sensitivity shear-force detections, elastic energy acquisition, and other related fields, which have important application prospects and can bring new research ideas to the above fields.

Appendix A. The dimension number of the fractal lattice and the topological states

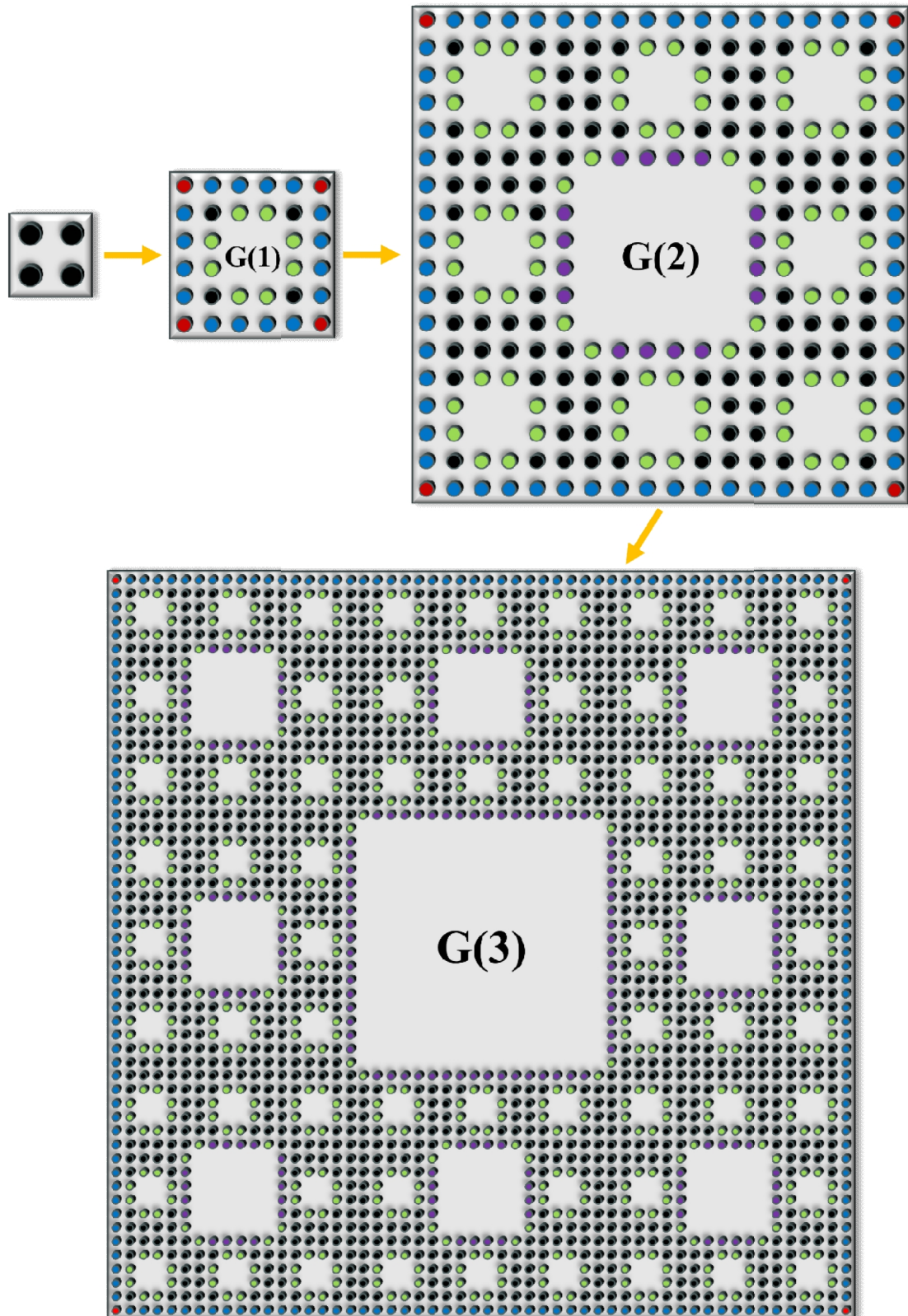


Fig.A1. The smallest cell in the fractal structure has four grid points, and the box counting method is used to calculate the dimensions of the structure. The first generation $G(1)$ has eight minimal cells, the second generation $G(2)$ contains eight $G(1)$, and $G(3)$ contains another eight $G(2)$, or for 64 $G(1)$, which shows that there will be eight $G(n)$ generations of the square fractal structure. The red, blue, purple, green, and black columns in the figure denote the outer corner state, the edge state, the inner edge state, the inner corner state, and the body state, respectively.

The box-counting method is used to calculate the dimension number of fractal lattices[33]. As can be seen from Fig.A1, the total number of boxes in each generation is $N_{G_n} = 4 \times 8^n$, and the number of transverse boxes is $N_L = 2 \times 3^n$, so the fractal dimension can be obtained:

$$\dim(D_G) = \lim_{n \rightarrow \infty} \frac{\ln(N_{G_n})}{\ln(N_L)} = \lim_{n \rightarrow \infty} \frac{\ln(4 \times 8^n)}{\ln(2 \times 3^n)} \approx 1.893 \quad (\text{A.1})$$

$$\dim(D_o) = \lim_{n \rightarrow \infty} \frac{\ln(N_c)}{\ln(N_L)} = \lim_{n \rightarrow \infty} \frac{\ln(4)}{\ln(2 \times 3^n)} = 0 \quad (\text{A.2})$$

$$\dim(D_i) = \lim_{n \rightarrow \infty} \frac{\ln(N_{ic})}{\ln(N_L)} = \lim_{n \rightarrow \infty} \frac{\ln(\sum_{i=1}^n 8^i)}{\ln(2 \times 3^n)} \approx 1.893 \quad (\text{A.3})$$

$$\dim(D_e) = \lim_{n \rightarrow \infty} \frac{\ln(N_e)}{\ln(N_L)} = \lim_{n \rightarrow \infty} \frac{\ln(8^n \times (3^n - 1) + \sum_{i=1}^{n-1} (3^i - 1) \times 8^{n-i})}{\ln(2 \times 3^n)} \approx 1.893, \quad (\text{A.4})$$

where N_c, N_i, N_e are numbers of outer corner, inner corner and edge states, respectively. For the fractal lattice, the total states of $G(1)$ fractal lattice are 32, including 4 outer corner states, 8 inner corner states, and 16 edge states. For $G(2)$, the total box number is consistent with the total lattice number, which is 256. In the above calculation, it can be seen that there are 4 outer corner states, 72 inner corner states and 80 edge states, which is consistent with the calculation results in the Section 2.

Extending the fractal structure to an infinite space, the proportions of the numbers of inner corner, edge, and bulk states to the total number of modes generated in infinite iterations are:

$$\omega_{inner\ corner} = \lim_{n \rightarrow \infty} \frac{N_{ic}}{N_{G_n}} = \lim_{n \rightarrow \infty} \frac{\sum_{i=1}^n 8^i}{4 \times 8^n} = \frac{2}{7} \quad (\text{A.5})$$

$$\omega_{edge} = \lim_{n \rightarrow \infty} \frac{N_e}{N_{G_n}} = \lim_{n \rightarrow \infty} \frac{8^n \times (3^n - 1) + \sum_{i=1}^{n-1} (3^i - 1) \times 8^{n-i}}{4 \times 8^n} = \frac{4}{35} \quad (\text{A.6})$$

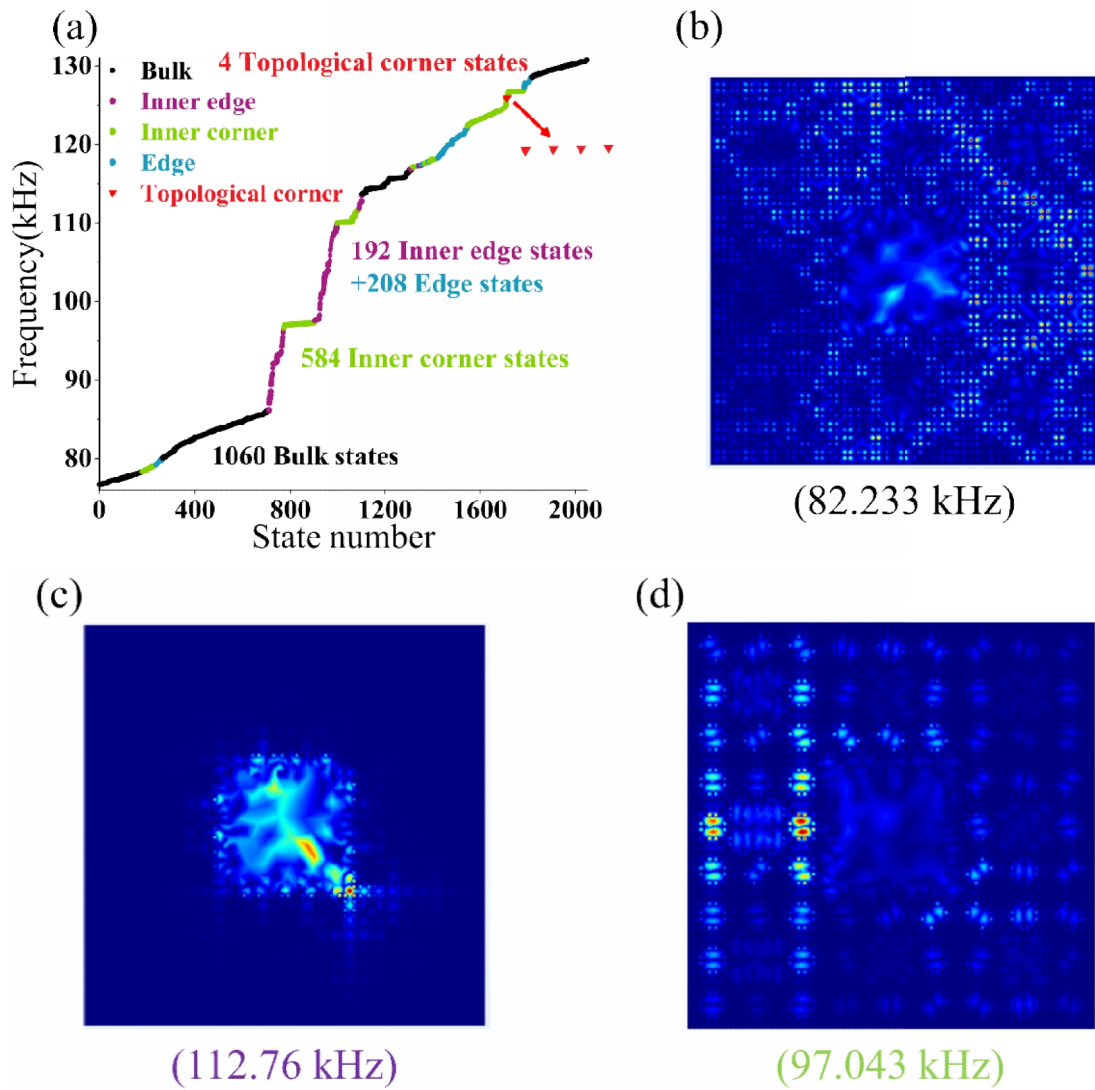
$$\omega_{bulk} = 1 - \omega_{inner\ corner} - \omega_{edge} = \frac{3}{5} \quad (\text{A.7})$$

Appendix B. Simulated eigenstates of the G(3) fractal model

The eigenstates of the G(3) generation square fractal structure are calculated. According to Appendix A, the total number of eigenstates in the G(3) generation structure is 2048, including 4 outer corner states, 584 inner corner states and 400 edge states. Fig.B1 shows the eigenstates of G(3) fractal structure obtained by numerical simulations. It is showed that there are 1060 bulk states (black), 584 inner corner states (green) and 400 edge states, which includes 192 inner edge states (purple) and 208 edge states (blue). The four topological corner states are represented by red inverted triangles. Displacement distributions of the G(3) fractal structure are shown in Fig.B1 (b)-(d). It is shown that there appears bulk state (82.233 kHz), inner edge state (112.76 kHz), inner corner state (97.043

kHz), edge state(121.03 kHz) and topological corner state (125.94 kHz).

The energy of the corner state maintains a high concentration, and the frequency range of the calculated results of the generation G(3) structure is the same as that of the generation G(2), which is due to the excellent self-similarity of the fractal structure.



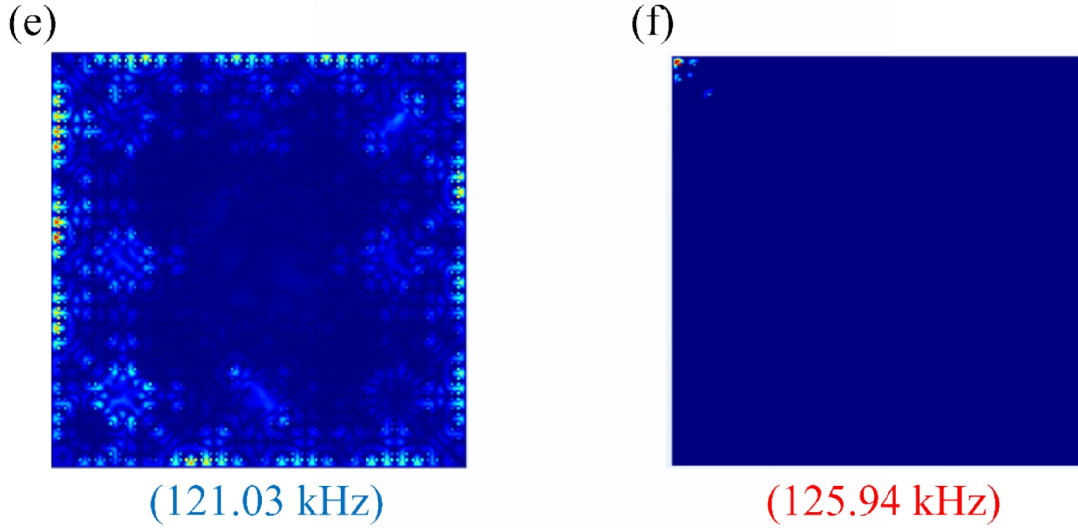
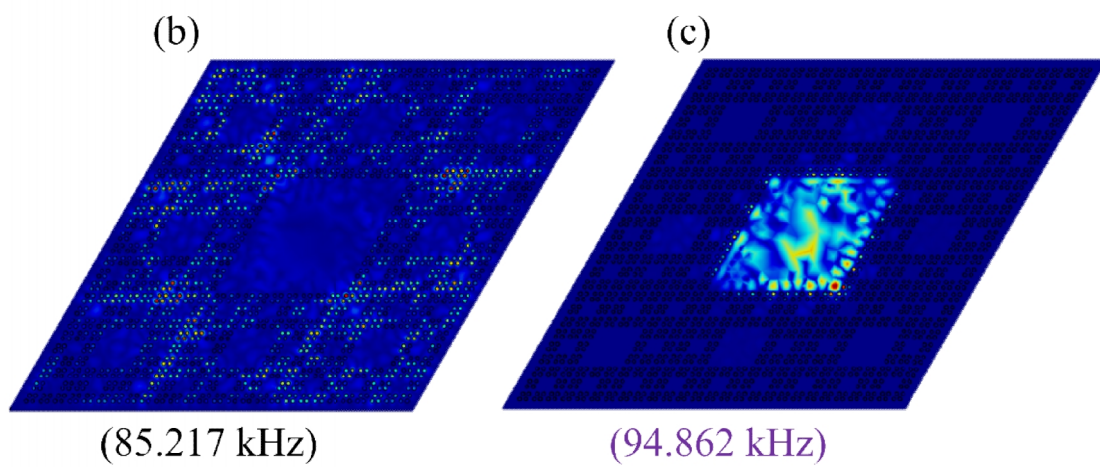
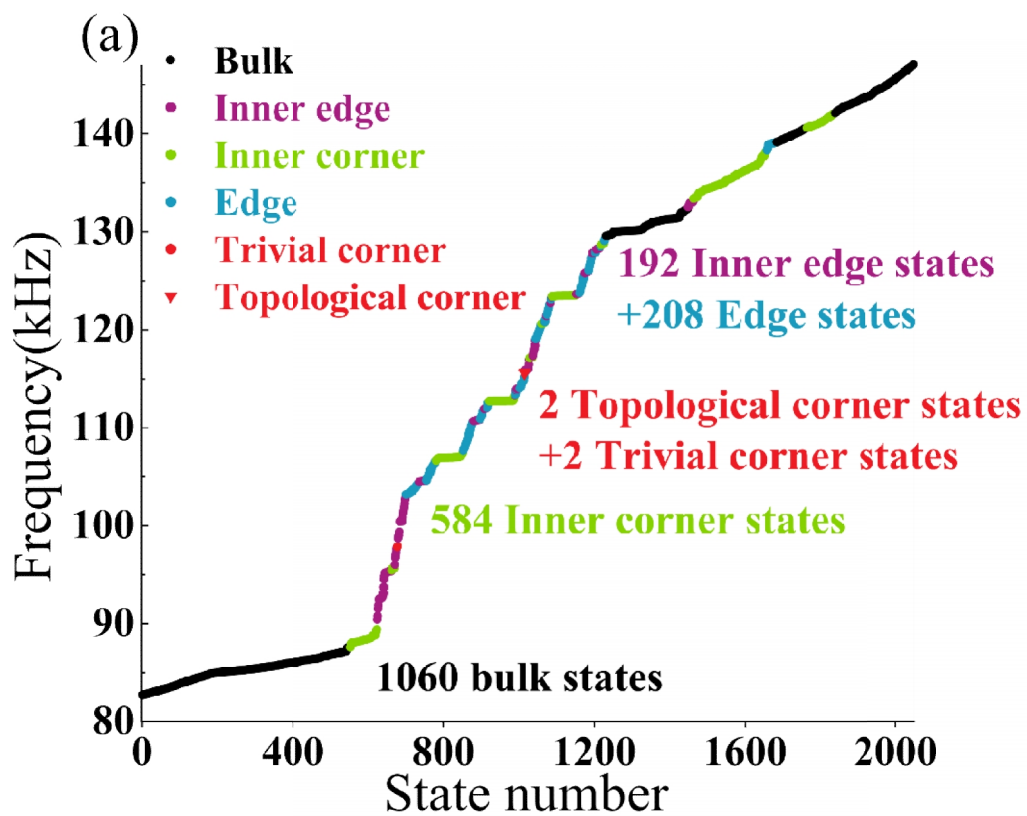


Fig.B1. (a) The eigenfrequency of the G(3) square fractal obtained by simulations at Bott index=1. Black, purple, green, blue and red dots denote the bulk states, inner edge states, inner corner states, edge states and topological corner states, respectively. (b)-(f) denote displacement distributions of the bulk state at 82.233 kHz, the inner edge state at 112.76 kHz, the inner corner state at 97.043 kHz, the edge state at 121.03 kHz and the topological corner state at 125.94 kHz, respectively.

Fig.B2 shows the eigenstates of the G(3) generation elastic rhomboid fractal lattice, and the number of states is consistent with the calculated fractal dimension number. In Fig.B2(a), the topological corner states, trivial corner states, edge states, and inner edge states, inner corner states and bulk states are shown with different colors. Fig.B2 (b-d) shows displacement distributions of the bulk state (85.217 kHz), inner edge state (94.862 kHz), inner corner state (112.77 kHz), and edge state (126.94 kHz), trivial corner state (97.908 kHz) and topological corner state (115.83 kHz) obtained by simulations. It is shown that the energy of the corner and edge states remain highly concentrated.



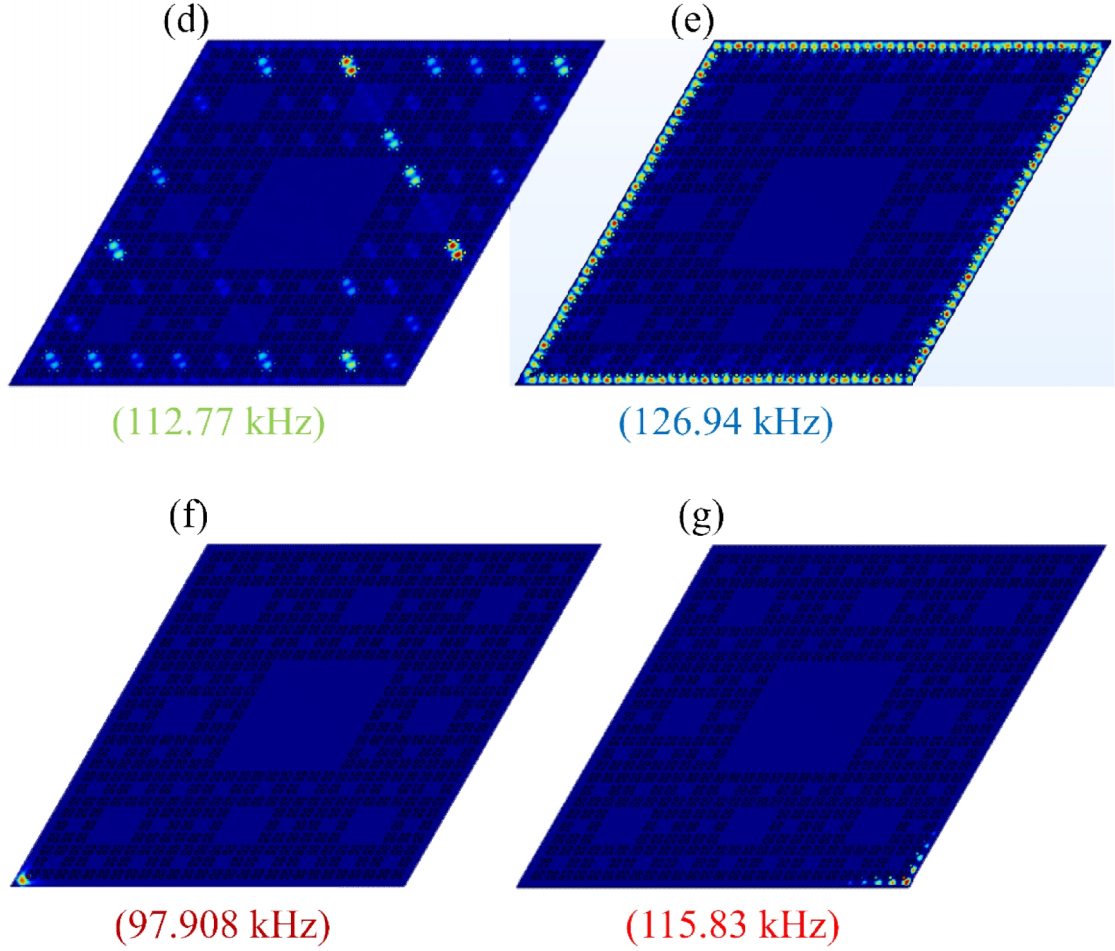


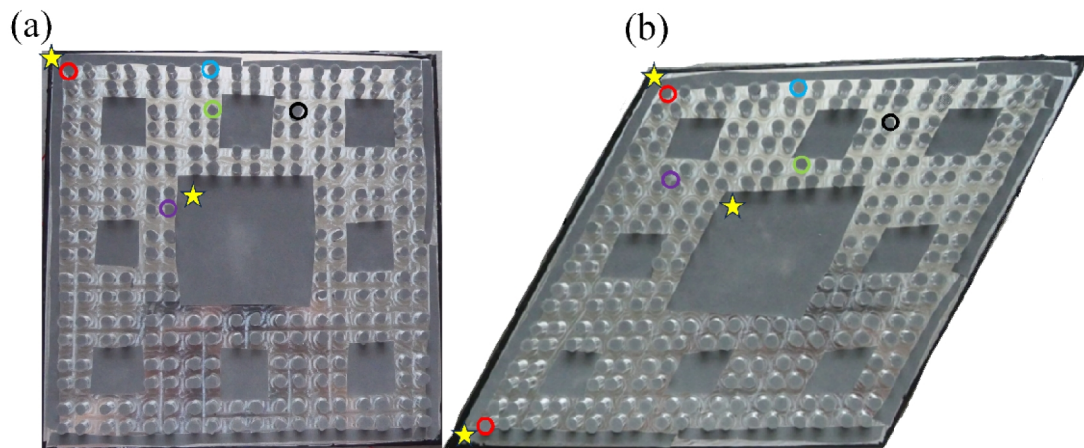
Fig.B2. The eigenfrequency of the G(3) rhombus fractal obtained by simulations at Bott index=1. Black, purple, green, blue and red denote the bulk state, inner edge state, inner corner state, edge state, trivial corner state and topological corner state, respectively. (b)-(f) displacement distributions of the bulk state (85.217 kHz), inner edge state (94.862 kHz), inner corner state (112.77 kHz), edge state (126.94 kHz), trivial corner state (97.908 kHz) and topological corner state (115.83 kHz), respectively.

Appendix C. Experimental samples and experimental platform

The fabricated fractal samples are shown in Fig. 6(a)-(b), made of aluminum ($\rho = 2700\text{kg/m}^3$, $\nu = 0.33$, $E = 68.9\text{GPa}$). The exciter is located at the position of the yellow pentagram shown in Fig. 6(a). Five types of topological corner, edge, inner edge, inner corner, and bulk state

are marked with red, blue, purple, green, and black circles respectively to measure the response spectrum.

The experimental test platform is shown in Fig. C1(a) and (b). Periodic sinusoidal wave signals with frequencies from 80 kHz to 140 kHz are generated by using a signal generator, which is then amplified by a power amplifier (B&K 2706) to drive the piezoelectric exciter (a PZT resonator with a radius of 5 mm). The scanning laser vibrometer (PSV-500, POLYTEC) is used to measure the out-of-plane velocities at selected points throughout the region, which is then transmitted to the vibrometer controller and converted into a displacement signal. The vibration absorbing glue is applied around the sample to ensure that the energy is not excessively dissipated.



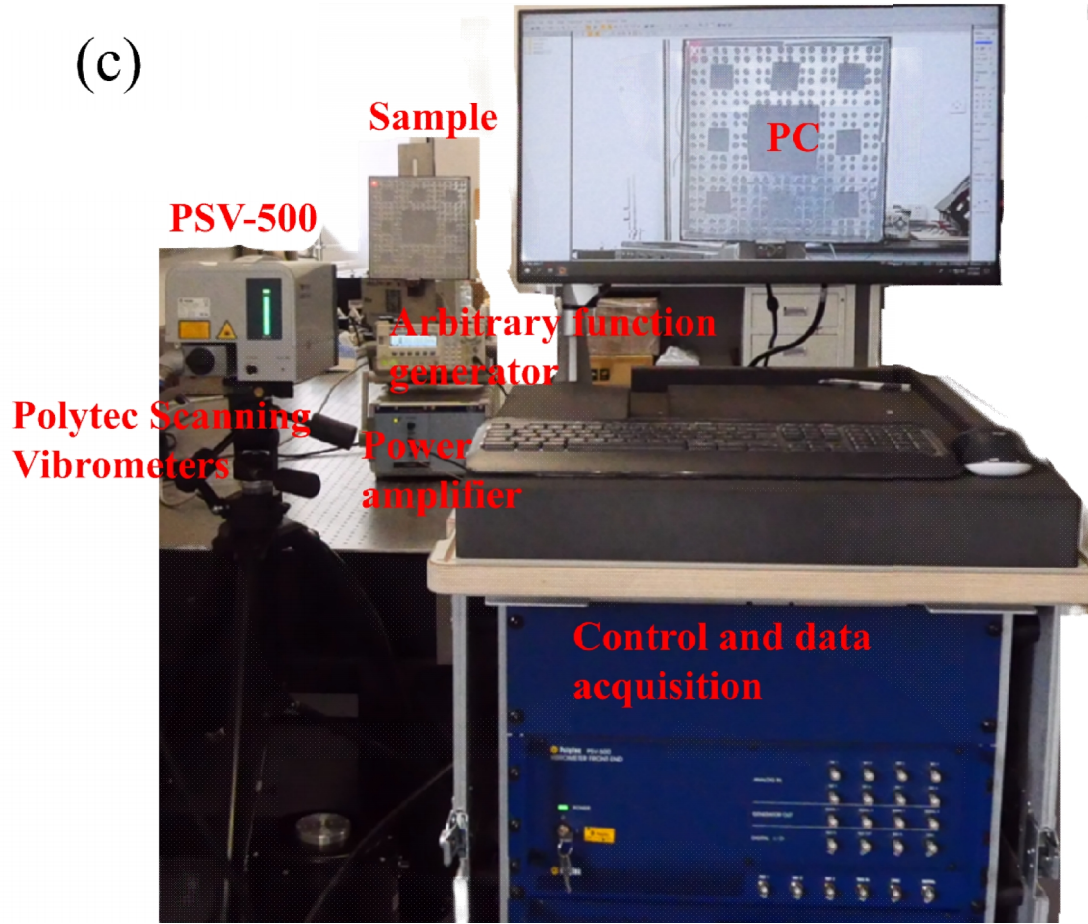


Fig.C1. Elastic fractal samples and experimental platform. (a) and (b) Fabricated square and rhombus fractal samples, respectively. The yellow pentagram represents the position of the piezoelectric exciter, and red, blue, purple, green and black points indicate the positions of the outer corner state, boundary state, inner edge state, inner corner state and body state, respectively. (c) the experimental platform

Appendix D. Simulation of eigenstates of periodic elastic structures

In order to verify further the superiority of fractal structures in elastic system, square and rhombus periodic structures with an integer dimension are designed, and the coupling parameters (the intracellular coupling is greater than the extracellular coupling) and other parameters of the structure are consistent with the fractal structures. It is found that the square structure has 24 edge states, 4 topological corner states, and

the rest are bulk states as shown in Fig.D1(a). In the trivial state, only bulk states emerged, as shown in Fig.D1(b). Fig.D1(c)-(e) shows displacement distributions of the bulk state(82.629 kHz) 、 edge states(120.54 kHz)、 topological corner state(125.47 kHz), the frequency of which are close to those in the fractal structure. The calculation results of the rhombus structure shows that in the topological state, 51 edge states, 2 topological corner states and 2 trivial corner states appear, and the rest are bulk states, as shown in Fig.D2(a). In the trivial state, only bulk states emerged, as shown in Fig.D2(b). Fig.D2 (c)-(f) shows displacement distributions of the bulk state (85.325 kHz), edge state(126.8 kHz), trivial corner states(98.05 kHz), and topological corner states(115.83 kHz), and the frequency of each state is close to the that in the fractal structure. However, different from the fractal structure, there is no inner corner state and inner edge state in the periodic structure, and due to the disappearance of the self-similarity of the structure, the periodic structure has far fewer edge states than the fractal structure. The number of edge states in the fractal structure is 80, while the number of square edge states in the integer dimension is only 24. By comparing the elastic fractal structure with the elastic periodic structure, it is proved that the elastic fractal structure has a great advantage in the number of corner states, which is much more than that of the periodic structure.

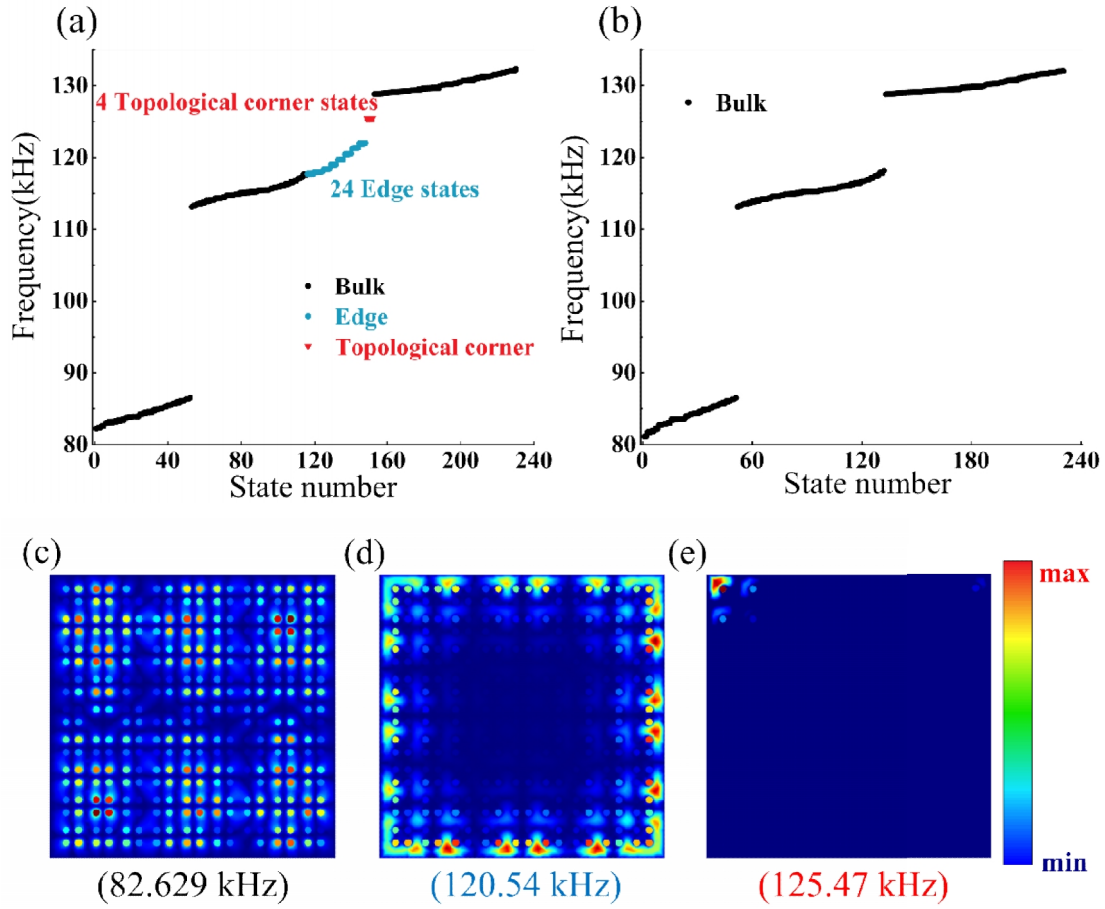
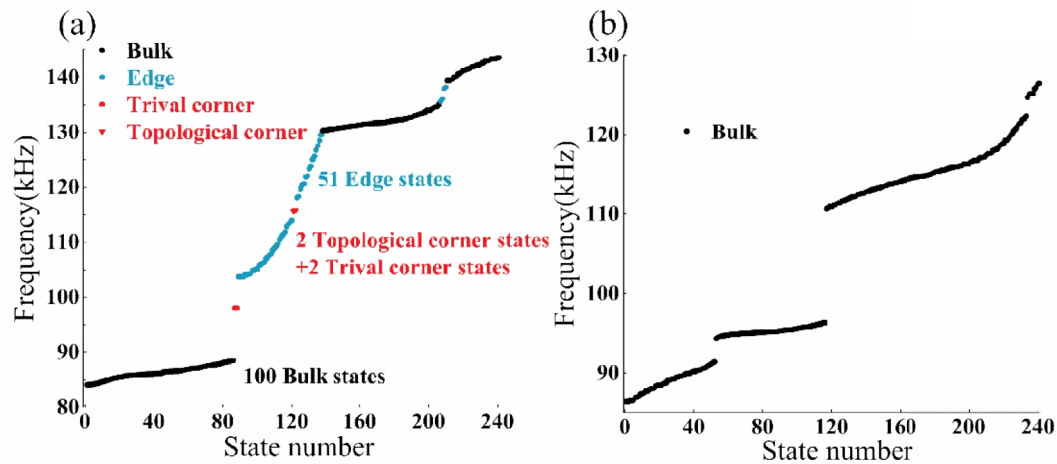


Fig.D1. The eigenstates of the periodic square structure obtained by simulations. Red inverted triangles, blue dots and black dots denote topological corner states, edge states and bulk states, respectively. (a) Eigenfrequency of the periodic square structure under the coupling parameters where topology occurs. (b) Eigenfrequency of the periodic square structure under the coupling parameters where no topology occurs. (c)-(e) Displacement distributions of the bulk state at 82.629 kHz, the edge states at 120.54 kHz and the topological corner state at 125.47 kHz.



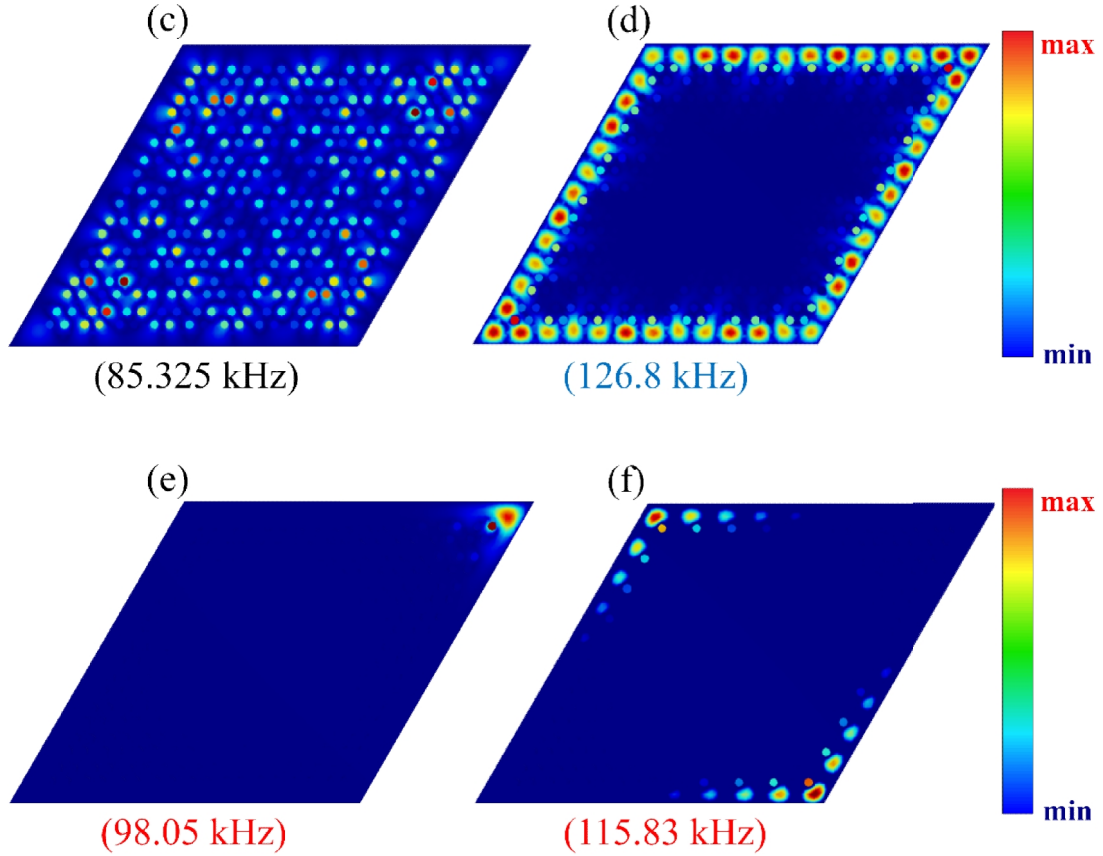
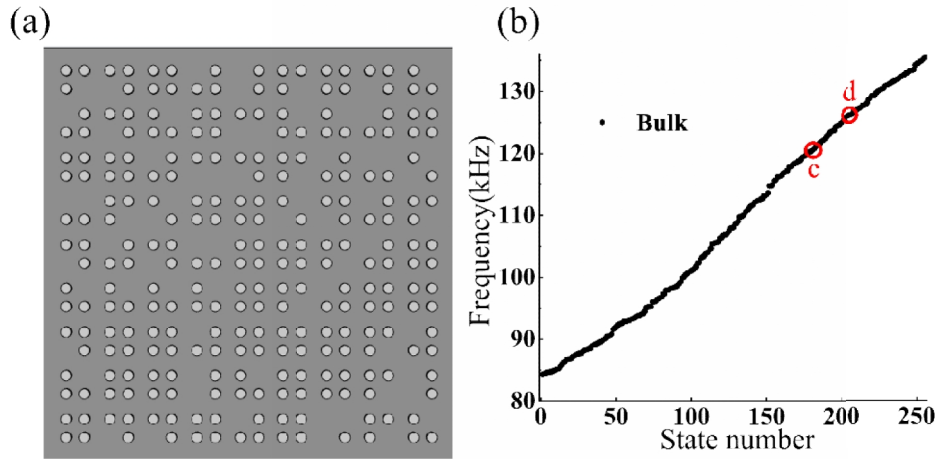


Fig.D2. The eigenstates of the periodic rhombus structure obtained by simulations. Red inverted triangles, red dots, blue dots and black dots denote topological corner states, trivial corner states, edge states and bulk states, respectively. (a) Eigenfrequency of the periodic rhombus structure under the coupling parameters where topology occurs. (b) Eigenfrequency of the periodic rhombus structure under the coupling parameters where no topology occurs. (c)-(e) Displacement distributions of the bulk state at 85.325 kHz, the edge states at 126.8 kHz, the trivial corner state at 98.05 kHz and the topological corner state at 115.83 kHz, respectively.

Appendix E. Non-fractal models

Eigenstates of fractal and non-fractal elastic systems are compared and the differences are checked. As shown in Fig. 9(a), for the non-fractal structure, 68 lattice points are randomly removed from the square fractal model with integer-dimensions and 256 lattice points are remained. Simulations are carried out to obtain the eigenstates, the results are shown

in Fig. 9(b). It can be seen from the spectrum diagram of the non-fractal structure that there appears no topological corner state and there is no eigenstate bandgap. Displacement distributions at the corner state frequency of the fractal structure are tested, and the results are shown in Fig. 9(c)-(d). It can be seen that there are no obvious edge states and corner states, indicating that there is no a topological state for the non-fractal structure. The above operations are also carried out for the rhomboid structure, the results are shown in Fig. 10. Similarly, it is shown that no obvious edge and corner states appear. The results show that occurrence of the topological corner states of fractal structures in elastic systems are owing to the special structures.



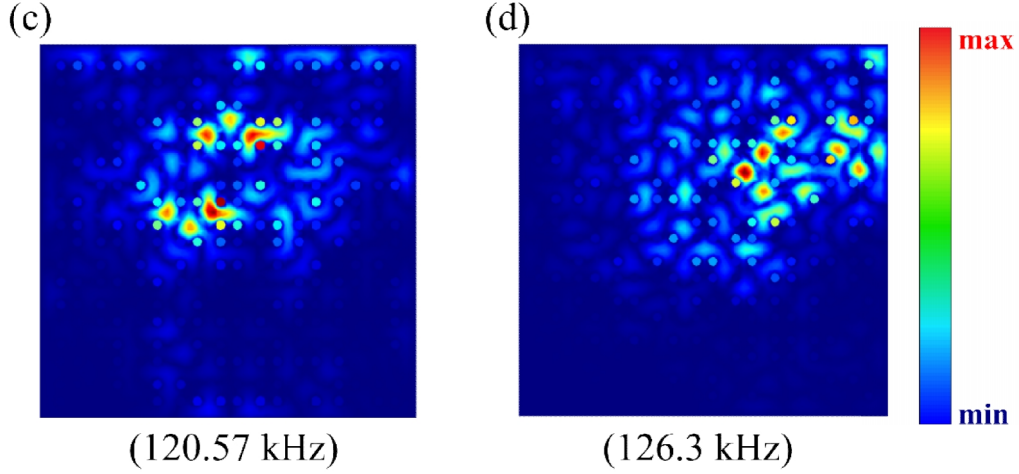


Fig.E1. Characteristics of non-fractal square elastic plate. (a) Diagram of non-fractal square elastic plate (some lattice points are deleted randomly) (b) Eigenfrequency of the square non-fractal structure calculated by simulations. (c)-(d) Displacement of the bulk state at 120.57 kHz and 126.3 kHz.

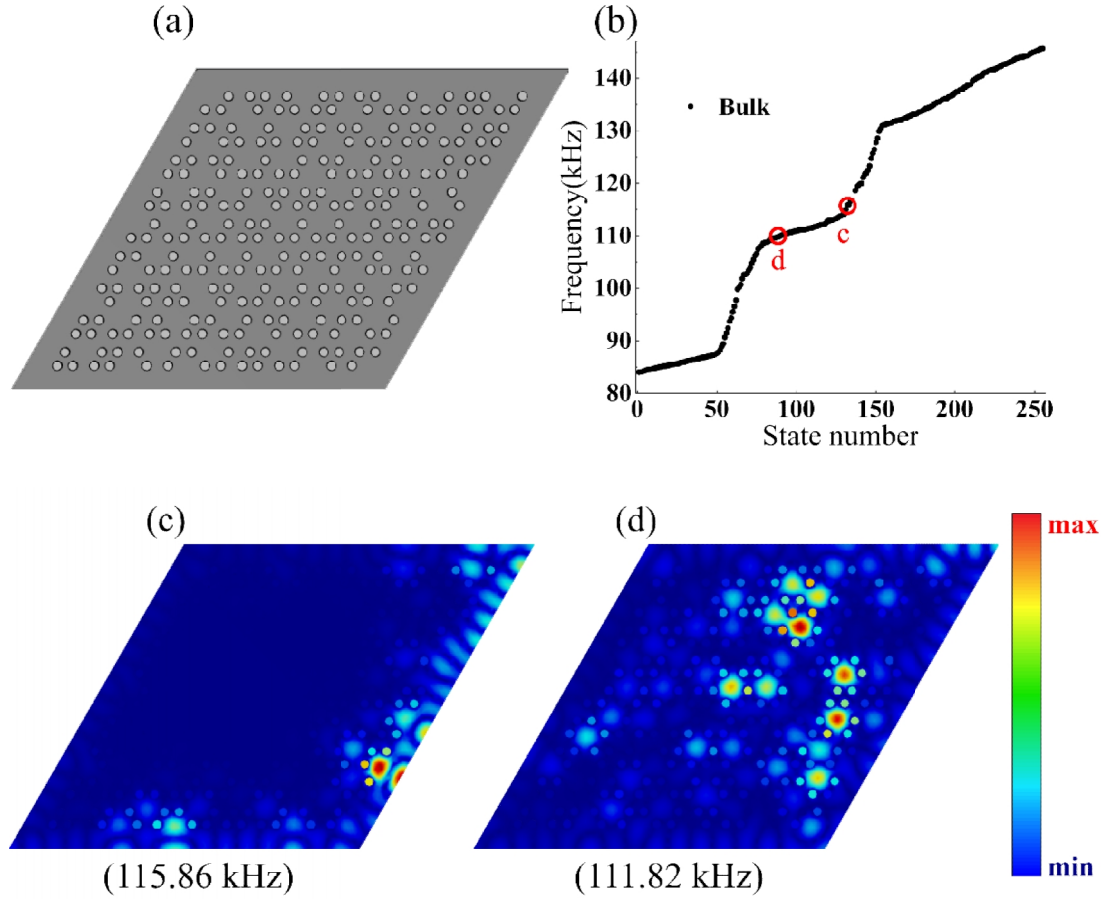


Fig.E2. Characteristics of non-fractal rhombus elastic plate. (a) Diagram of non-fractal rhombus elastic plate (some lattice points are deleted randomly) (b) Eigenfrequency of the rhombus non-fractal structure calculated by simulations. (c)-(d) Displacement of the bulk state at 115.86 kHz and 111.82 kHz.

Appendix F. Topological index

In reference[18,46,47], a topological index was introduced to explain the difference in position between topological and trivial corner states in rhomboid plates. This index captures the interaction between the bulk Hamiltonian topology and the defect topology. The topological indexes are calculated to differentiate the topological and trivial corner states. It can be seen that at the $\pi/3$ corner in the diamond structure, $N_+ = 1$ and $N_- = 1$, the topological index $N = 0$. At the $2\pi/3$ corner, $N_+ = 1$ and $N_- = 2$, the topological index $N = 1$, which indicates the occurrence of the stable mode, namely, topological protection is generated. Thus, for the rhomboid structure in this work, the topological protection occurs at the $2\pi/3$ corner.

Appendix G. Experimental verification of trivial corner states

In order to prove that the corner state at the $\pi/3$ corner of the rhomboid structure is trivial, experimental robustness verifications are conducted on the $\pi/3$ corner of the rhomboid elastic plate. The defects are set at the corner and disorders are introduced to observe whether there is robustness, which is shown in the inset of **Fig.G1**. Displacement distributions are shown in **Fig.G1**. It is found that after defects and disorders are introduced, the corner state appearing at the $\pi/3$ corner does not maintain the energy concentration, and the energy spreads

around, namely there is no robustness. Thus, the corner state appearing at the $\pi/3$ corner of the rhomboid fractal structure is indeed a trivial corner state.

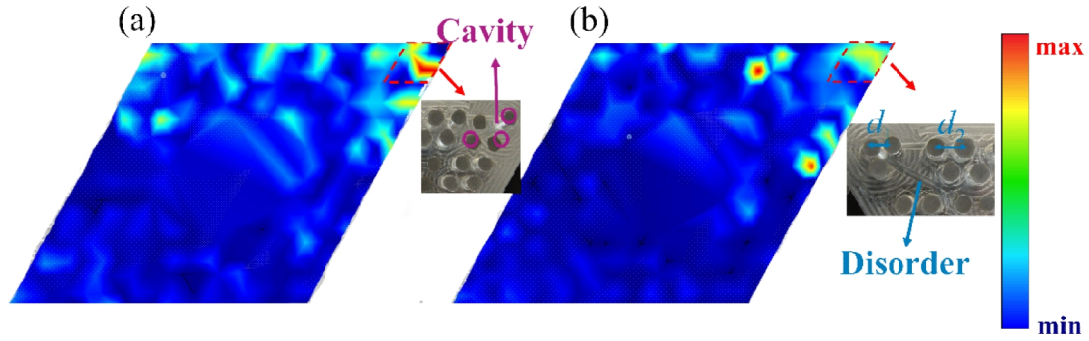


Fig.G1. Experimental verification of the absence of topological protection at $\pi/3$ corners. (a) model with cavity (b) model with disorder.

References

- [1] K. von Klitzing, The quantized Hall effect, *Rev Mod Phys.* 58 (1986) 519–531. <https://doi.org/10.1103/RevModPhys.58.519>.
- [2] M.Z. Hasan, C.L. Kane, *Colloquium* : Topological insulators, *Rev Mod Phys.* 82 (2010) 3045–3067. <https://doi.org/10.1103/RevModPhys.82.3045>.
- [3] A.B. Khanikaev, S. Hossein Mousavi, W.-K. Tse, M. Kargarian, A.H. MacDonald, G. Shvets, Photonic topological insulators, *Nat Mater.* 12 (2013) 233–239. <https://doi.org/10.1038/nmat3520>.
- [4] A.B. Khanikaev, G. Shvets, Two-dimensional topological photonics, *Nat Photonics.* 11 (2017) 763–773. <https://doi.org/10.1038/s41566-017-0048-5>.
- [5] L.-H. Wu, X. Hu, Scheme for Achieving a Topological Photonic Crystal by Using Dielectric Material, *Phys Rev Lett.* 114 (2015) 223901. <https://doi.org/10.1103/PhysRevLett.114.223901>.
- [6] Z. Wang, Y. Chong, J.D. Joannopoulos, M. Soljačić, Observation of unidirectional backscattering-immune topological electromagnetic states, *Nature.* 461 (2009) 772–775. <https://doi.org/10.1038/nature08293>.
- [7] Z. Yang, F. Gao, X. Shi, X. Lin, Z. Gao, Y. Chong, B. Zhang, Topological Acoustics, *Phys Rev Lett.* 114 (2015) 114301. <https://doi.org/10.1103/PhysRevLett.114.114301>.
- [8] B.-Z. Xia, T.-T. Liu, G.-L. Huang, H.-Q. Dai, J.-R. Jiao, X.-G. Zang, D.-J. Yu, S.-J. Zheng, J. Liu, Topological phononic insulator with robust pseudospin-dependent transport, *Phys Rev B.* 96 (2017) 094106. <https://doi.org/10.1103/PhysRevB.96.094106>.

- [9] R. Fleury, A.B. Khanikaev, A. Alù, Floquet topological insulators for sound, *Nat Commun.* 7 (2016) 11744. <https://doi.org/10.1038/ncomms11744>.
- [10] J. Lu, C. Qiu, M. Ke, Z. Liu, Valley Vortex States in Sonic Crystals, *Phys Rev Lett.* 116 (2016) 093901. <https://doi.org/10.1103/PhysRevLett.116.093901>.
- [11] M. Xiao, G. Ma, Z. Yang, P. Sheng, Z.Q. Zhang, C.T. Chan, Geometric phase and band inversion in periodic acoustic systems, *Nat Phys.* 11 (2015) 240–244. <https://doi.org/10.1038/nphys3228>.
- [12] Q. Wu, H. Chen, X. Li, G. Huang, In-Plane Second-Order Topologically Protected States in Elastic Kagome Lattices, *Phys Rev Appl.* 14 (2020). <https://doi.org/10.1103/PhysRevApplied.14.014084>.
- [13] Z. Zheng, J. Yin, J. Wen, D. Yu, Higher-order topological states in locally resonant elastic metamaterials, *Appl Phys Lett.* 120 (2022). <https://doi.org/10.1063/5.0074463>.
- [14] Y. Chen, J. Li, J. Zhu, Topology optimization of quantum spin Hall effect-based second-order phononic topological insulator, *Mech Syst Signal Process.* 164 (2022). <https://doi.org/10.1016/j.ymssp.2021.108243>.
- [15] J. Xu, Y. Zheng, T. Ma, H. Chen, B. Wu, J. Wang, S. Li, I. Kuznetsova, I. Nedospasov, J. Du, H. Shi, D. Chen, F. Sun, Realization of Topological Valley Hall Edge States of Elastic Waves in Phononic Crystals Based on Material Differences, *Phys Rev Appl.* 19 (2023). <https://doi.org/10.1103/PhysRevApplied.19.034062>.
- [16] S.Y. Yu, C. He, Z. Wang, F.K. Liu, X.C. Sun, Z. Li, H.Z. Lu, M.H. Lu, X.P. Liu, Y.F. Chen, Elastic pseudospin transport for integratable topological phononic circuits, *Nat Commun.* 9 (2018). <https://doi.org/10.1038/s41467-018-05461-5>.
- [17] S.H. Mousavi, A.B. Khanikaev, Z. Wang, Topologically protected elastic waves in phononic metamaterials, *Nat Commun.* 6 (2015). <https://doi.org/10.1038/ncomms9682>.
- [18] H. Fan, B. Xia, L. Tong, S. Zheng, D. Yu, Elastic Higher-Order Topological Insulator with Topologically Protected Corner States, *Phys Rev Lett.* 122 (2019). <https://doi.org/10.1103/PhysRevLett.122.204301>.
- [19] F. Hong, K. Zhang, L. Qi, B. Ding, Z. Deng, High-frequency topological corner and edge states in elastic honeycomb plates, *Int J Mech Sci.* 246 (2023). <https://doi.org/10.1016/j.ijmecsci.2023.108141>.
- [20] Y. Liu, B. Lei, P. Yu, L. Zhong, K. Yu, Y. Wu, Second-order topological corner states in two-dimensional elastic wave metamaterials with nonsymmorphic symmetries, *Mech Syst Signal Process.* 198 (2023). <https://doi.org/10.1016/j.ymssp.2023.110433>.
- [21] M.F. Goodchild, D.M. Mark, The Fractal Nature of Geographic Phenomena, *Annals of the Association of American Geographers.* 77 (1987) 265–278. <https://doi.org/10.1111/j.1467-8306.1987.tb00158.x>.
- [22] S. Manna, S. Nandy, B. Roy, Higher-order topological phases on fractal lattices, *Phys Rev B.* 105 (2022). <https://doi.org/10.1103/PhysRevB.105.L201301>.
- [23] S.N. Kempkes, M.R. Slot, S.E. Freeney, S.J.M. Zevenhuizen, D. Vanmaekelbergh, I. Swart, C.M. Smith, Design and characterization of electrons

- in a fractal geometry, *Nat Phys.* 15 (2019) 127–131. <https://doi.org/10.1038/s41567-018-0328-0>.
- [24] S. Pai, A. Prem, Topological states on fractal lattices, *Phys Rev B.* 100 (2019). <https://doi.org/10.1103/PhysRevB.100.155135>.
- [25] T. Biesenthal, L.J. Maczewsky, Z. Yang, M. Kremer, M. Segev, A. Szameit, M. Heinrich, Fractal photonic topological insulators, n.d. <https://www.science.org>.
- [26] Z. Yang, E. Lustig, Y. Lumer, M. Segev, Photonic Floquet topological insulators in a fractal lattice, *Light Sci Appl.* 9 (2020). <https://doi.org/10.1038/s41377-020-00354-z>.
- [27] S. Zheng, X. Man, Z.L. Kong, Z.K. Lin, G. Duan, N. Chen, D. Yu, J.H. Jiang, B. Xia, Observation of fractal higher-order topological states in acoustic metamaterials, *Sci Bull (Beijing)*. 67 (2022) 2069–2075. <https://doi.org/10.1016/j.scib.2022.09.020>.
- [28] J. Li, Y. Sun, Q. Mo, Z. Ruan, Z. Yang, Fractality-induced topological phase squeezing and devil’s staircase, *Phys Rev Res.* 5 (2023). <https://doi.org/10.1103/physrevresearch.5.023189>.
- [29] J. Li, Q. Mo, J.H. Jiang, Z. Yang, Higher-order topological phase in an acoustic fractal lattice, *Sci Bull (Beijing)*. 67 (2022) 2040–2044. <https://doi.org/10.1016/j.scib.2022.09.024>.
- [30] B. Ren, Y. V. Kartashov, L.J. Maczewsky, M.S. Kirsch, H. Wang, A. Szameit, M. Heinrich, Y. Zhang, Theory of nonlinear corner states in photonic fractal lattices, *Nanophotonics*. (2023). <https://doi.org/10.1515/nanoph-2023-0443>.
- [31] X.Y. Xu, X.W. Wang, D.Y. Chen, C.M. Smith, X.M. Jin, Quantum transport in fractal networks, *Nat Photonics.* 15 (2021) 703–710. <https://doi.org/10.1038/s41566-021-00845-4>.
- [32] Y. Xie, L. Song, W. Yan, S. Xia, L. Tang, D. Song, J.W. Rhim, Z. Chen, Fractal-like photonic lattices and localized states arising from singular and nonsingular flatbands, *APL Photonics.* 6 (2021). <https://doi.org/10.1063/5.0068032>.
- [33] B.B. Mandelbrot, J.A. Wheeler, *The Fractal Geometry of Nature*, *Am J Phys.* 51 (1983) 286–287. <https://doi.org/10.1119/1.13295>.
- [34] Z. Zheng, J. Yin, J. Wen, D. Yu, X. Chen, Switchable corner states in phononic crystals realized by inverse design, *Int J Mech Sci.* 243 (2023). <https://doi.org/10.1016/j.ijmecsci.2022.108035>.
- [35] B.Y. Xie, G.X. Su, H.F. Wang, H. Su, X.P. Shen, P. Zhan, M.H. Lu, Z.L. Wang, Y.F. Chen, Visualization of Higher-Order Topological Insulating Phases in Two-Dimensional Dielectric Photonic Crystals, *Phys Rev Lett.* 122 (2019). <https://doi.org/10.1103/PhysRevLett.122.233903>.
- [36] B.Y. Xie, H.F. Wang, H.X. Wang, X.Y. Zhu, J.H. Jiang, M.H. Lu, Y.F. Chen, Second-order photonic topological insulator with corner states, *Phys Rev B.* 98 (2018). <https://doi.org/10.1103/PhysRevB.98.205147>.
- [37] Y. Chen, X. Liu, G. Hu, Topological phase transition in mechanical honeycomb lattice, *J Mech Phys Solids.* 122 (2019) 54–68. <https://doi.org/10.1016/j.jmps.2018.08.021>.

- [38] R. Zhao, G.-D. Xie, M.L.N. Chen, Z. Lan, Z. Huang, W.E.I. Sha, First-principle calculation of Chern number in gyrotropic photonic crystals, *Opt Express*. 28 (2020) 4638. <https://doi.org/10.1364/OE.380077>.
- [39] P. Wang, L. Lu, K. Bertoldi, Topological Phononic Crystals with One-Way Elastic Edge Waves, *Phys Rev Lett*. 115 (2015) 104302. <https://doi.org/10.1103/PhysRevLett.115.104302>.
- [40] S. Li, I. Kim, S. Iwamoto, J. Zang, J. Yang, Valley anisotropy in elastic metamaterials, *Phys Rev B*. 100 (2019) 195102. <https://doi.org/10.1103/PhysRevB.100.195102>.
- [41] Z.R. Liu, C.B. Hua, T. Peng, B. Zhou, Chern insulator in a hyperbolic lattice, *Phys Rev B*. 105 (2022). <https://doi.org/10.1103/PhysRevB.105.245301>.
- [42] A. Agarwala, V.B. Shenoy, Topological Insulators in Amorphous Systems, *Phys Rev Lett*. 118 (2017). <https://doi.org/10.1103/PhysRevLett.118.236402>.
- [43] H. Huang, F. Liu, Theory of spin Bott index for quantum spin Hall states in nonperiodic systems, *Phys Rev B*. 98 (2018). <https://doi.org/10.1103/PhysRevB.98.125130>.
- [44] M.A. Bandres, M.C. Rechtsman, M. Segev, Topological photonic quasicrystals: Fractal topological spectrum and protected transport, *Phys Rev X*. 6 (2016). <https://doi.org/10.1103/PhysRevX.6.011016>.
- [45] X.S. Wang, A. Brataas, R.E. Trancoso, Bosonic Bott Index and Disorder-Induced Topological Transitions of Magnons, *Phys Rev Lett*. 125 (2020). <https://doi.org/10.1103/PhysRevLett.125.217202>.
- [46] Z. Ma, Y. Liu, Y.X. Xie, Y.S. Wang, Tuning of Higher-Order Topological Corner States in a Honeycomb Elastic Plate, *Phys Rev Appl*. 19 (2023). <https://doi.org/10.1103/PhysRevApplied.19.054038>.
- [47] J. Noh, W.A. Benalcazar, S. Huang, M.J. Collins, K.P. Chen, T.L. Hughes, M.C. Rechtsman, Topological protection of photonic mid-gap defect modes, *Nat Photonics*. 12 (2018) 408–415. <https://doi.org/10.1038/s41566-018-0179-3>.